Politecnico di Torino
International University

von KARMAN INSTITUTE FOR FLUID DYNAMICS

Politecnico di Torino
Von Karman Institute for Fluid Dynamics

Department of Mechanical and Aerospace Engineering

Numerical investigation of downstream porosity for the reduction of turbulence–airfoil interaction noise

Author:
Umberto Bevilacqua

Supervisors:
Prof. Dr. Francesco Avallone
Politecnico di Torino

Dr. Andrea Piccolo
Delft University of Technology

Dr. Riccardo Zamponi
Delft University of Technology &
Von Karman Institute

Co-supervisor:
Dr. Sergi Pallejà Cabré
University of Southampton (ISVR)

A thesis submitted for the degree of
MSc Aerospace Engineering - Aerogasdynamics

March 31, 2026

«Se avete la possibilità di migliorare o migliorarvi in qualcosa, avete l'obbligo morale di farlo...»

Prof. Giuseppe Florio
Meccanica Razionale e Statistical Mechanics
Politecnico di Bari

«Scegliete la strada più difficile, più faticosa, possibilmente in salita, perché è dall'alto che si gode il panorama migliore.»

Enrico Brignano

Abstract

A numerical investigation has been conducted to characterize the reduction of noise emissions generated by a flat plate with downstream porosity interacting with incoming turbulence. The work builds on the experimental and analytical study performed at the University of Southampton, where several physical mechanisms potentially contributing to noise reduction were identified. These include inversions of the pressure-jump phase, possibly linked to secondary vorticity phenomena, destructive interference between noise sources, and alteration of coherent structures within the boundary layer. The numerical simulation was carried out using the Lattice–Boltzmann Method (LBM) solver PowerFLOW and was set up to reduce numerical effects on the interaction between turbulence and the flat plate, such as those caused by periodic boundary conditions. The analysis of the phase speed (acoustic velocity) and group speed (convective velocity) confirms the presence of evanescent acoustic waves in the near field, as suggested in the experimental study. In addition, the numerical results made it possible to observe phase inversions of the pressure jump by comparing the hydrodynamic pressure jump at the leading edge with that measured inside the porous region. This mechanism showed clear reduction peaks at integer Strouhal numbers, consistent with the experimental far-field measurements, and was linked to the breakup of spanwise vorticity. Although broader studies including additional configurations are required to generalize the observed physical mechanisms, these results represent a step forward in understanding the noise-reduction mechanisms associated with downstream porosity.

Contents

List of Figures

List of Tables

Chapter 1

Introduction

" Oppenheimer: Albert, when I came to you with those calculations... we thought we might start a chain reaction that would destroy the entire world.
Einstein: I remember it well. What of it?
Oppenheimer: I believe we did. "

— Oppenheimer (2023) — Final Scene

Millions of people across Europe are subjected to increasing noise pollution and the effects on public health are clear evidence of its impact.
A general framework for understanding this phenomenon is provided by the "Environmental Noise in Europe 2025" report [22], a document compiled every five years and now in its third edition.
According to this report, it is estimated that approximately 112 million people — more than 20% of the population in Europe — are exposed to long-term noise levels from road, rail, and aircraft sources that exceed the thresholds set by the Environmental Noise Directive (END). When considering the stricter limits established by the World Health Organization (WHO), this figure rises to approximately 150 million people. Italy, positioned in an intermediate range, measures approximately 25% of exposed people.
Based on the findings reported in the European study and confirming the analysis previously conducted by WHO Regional Office for Europe and Joint Research Centre [71], the effects of transport-related noise pollution are not limited to mere annoyance but extend to severe cardiovascular, mental, and metabolic diseases, which in 2021 alone led to the deaths of 66,000 people.
The problem of noise pollution is widespread. Unhealthy levels of noise pollution are experienced across all European countries. Road traffic is identified as the dominant source of environmental noise, and based on END thresholds, road transport accounts for around 92 million people exposed to it. This value has further worsened because the migration of the population from rural to urban areas over the past 50 years—increasing from 33.6% to 54.3%—resulted in the rapid development of cities, as reported in The World Bank [66]. In comparison, railway noise affects around 15 million people while aircraft noise impacts around 2.6 million (day-evening-night) and fewer than 1 million during the night. While rail and aircraft noise affect fewer people overall, they remain significant sources of local noise pollution, particularly near major rail transport corridors and airports. Such a localized issue also generates significant social inequity induced by the depreciation of properties located in those areas, as highlighted in both the most recent report and the previous quinquennial report [21].

In recent years, there has been a considerable commitment from national and international regulatory bodies toward pollution control, including noise pollution. These bodies have faced a significant challenge: noise is not merely a health-related issue, but also encompasses environmental, transport, urban planning, and road safety dimensions as cited by European Commission et al. [20].
However, it is well known that the working framework, created by Brown and van Kamp [6] for managing legislation on the reduction of noise emissions, is based on giving importance to human health. According to the most recent global trends, noise pollution fits into the 2030 Agenda for Sustainable Development. From this perspective, Europe, through the "Zero Pollution Action

Plan," has set the goal of a drastic reduction in pollution by 2050. This is achievable through a first intermediate result planned for 2030, which includes reducing the share of people chronically disturbed by transport noise by 30% [19], including aviation noise. The 2030 forecasts provide both a conservative and an optimistic scenario for road, rail, and air transport. Focusing on aviation, European Environment Agency [22] estimates that the number of people HA (Highly Annoyed) by aircraft noise is projected to decrease significantly, by up to 41% under the optimistic scenario and 32% in the conservative scenario, as shown in Figure 1.1. In parallel with these two types of

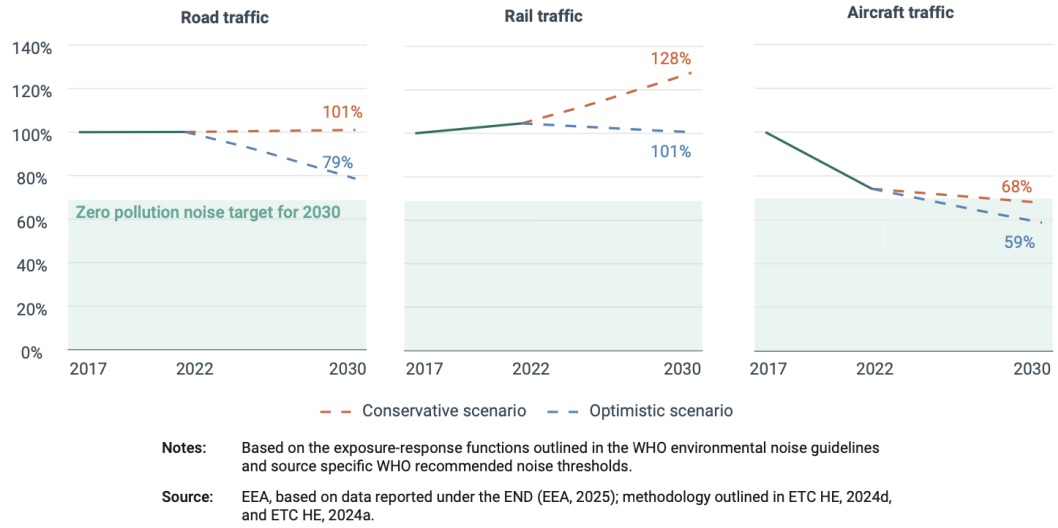

Figure 1.1: Projected percentage change from 2017 baseline to 2030 in the share of people highly annoyed by noise from rail, road and aircraft under a conservative and an optimistic scenario [22]

forecasts, the methodologies for achieving them are summarized in Figure 1.2. It is evident that making aircraft quieter is an essential prerequisite in both the short and long term.

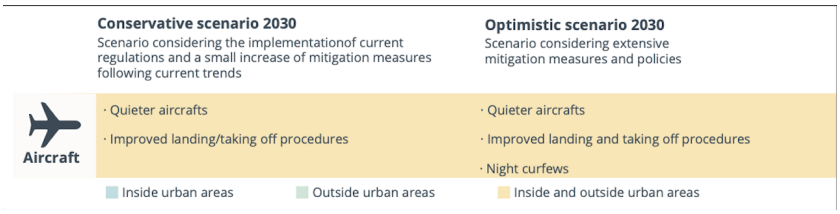

Figure 1.2: Overview of measures and degree of implementation for each source of transport noise included in the conservative and optimistic scenarios [22]

1.1 From turbojet to turbofan: acoustic emission

Even though the use of aircraft had been widespread since the 1920s with the first generation of piston and propeller-powered aircraft, noise emission issues began to intensify significantly with the advent of powerful first-generation jet engines. In the late 1950s, with the advent of the first jetliners equipped with four turbojet engines, such as the Boeing 707 and Douglas DC-8, noise became a primary concern, as reported by Leishman [43]. These larger and faster aircraft also increased the number of passengers, resulting in a rise in takeoffs and landings at major airports, much to the chagrin of those living or working nearby. "Hush kits" (the most common type being the "multi-lobe exhaust mixer" shown in Figure 1.3) were among the first techniques used to reduce noise emissions on older turbojet and low-bypass turbofan engines, as these engines are significantly louder than modern high-bypass turbofan engines as in figure 1.5b

Despite having a lower acoustic impact, modern high-bypass aircraft (such as the A380) exhibit an extremely complex and noisy distribution of acoustic sources, as shown in Figure 1.4, where tonal or broadband noise sources are quantified by their contribution to the total emission both in

(a) **Hush kit** mixer on the turbojet General Electric CJ805

(b) The IAE V2500 on the A320 family, using a mixed exhaust

Figure 1.3: Examples of hush kits.

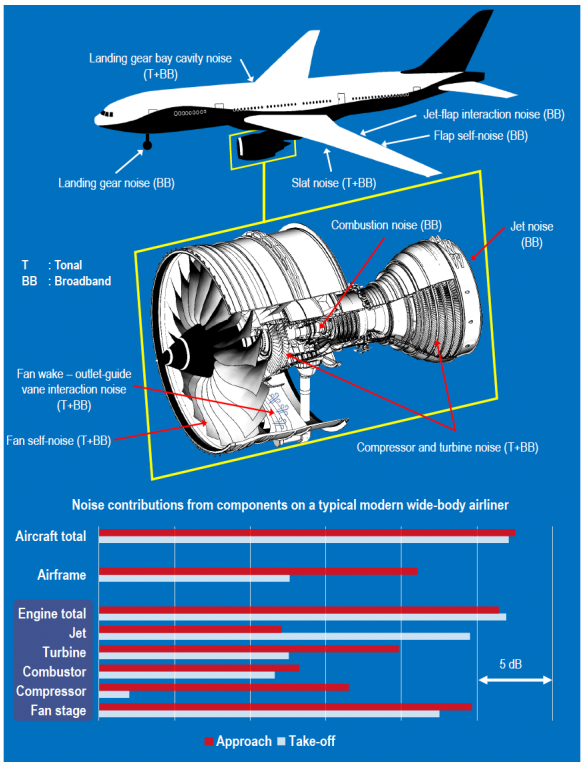

Figure 1.4: Focus on different type of noise emission [64]

take-off and approaching. The previously mentioned image highlights how most of the contribution to acoustic emission comes from the entire propulsion system (jet, turbine, combustor, fan), which is characterized by both tonal and broadband noise. Filippone [28] identifies the tonal component in the regular rotation of the propulsion system, while the broadband component is attributed to pressure fluctuations associated with various scales of turbulent flow. Jet and fan noise are the two primary acoustic sources in the propulsion system; however, their nature is extremely different.

Jet noise is purely broadband noise (see Figure 1.4) as it is linked to a high-speed (and subsonic) turbulent flow containing a wide range of length and time scales. This noise emission has decreased over the years following the construction of high-bypass ratio aircraft (as shown in figure 1.5b)—larger engines with lower exhaust velocities—in accordance with Lighthill's acoustic analogy, which estimates the acoustic intensity of a free jet (see Figure 1.5a) as shown in Equation 1.1:

$$\langle I(x)\rangle = \frac{\langle p'^2\rangle}{\rho_0 c_0} \sim \rho_0 c_0^3 \left(\frac{D}{|\mathbf{x}|}\right)^2 M^8 \sin^2(2\theta). \tag{1.1}$$

where $\langle p'^2\rangle$, ρ_0, c_0, D, M, and θ are respectively the root mean square (RMS) of the acoustic pressure, the density and speed of sound of the propagation medium, the jet diameter, the Mach

number, and the directivity angle. In the early 2000s, NASA conducted the first tests to implement

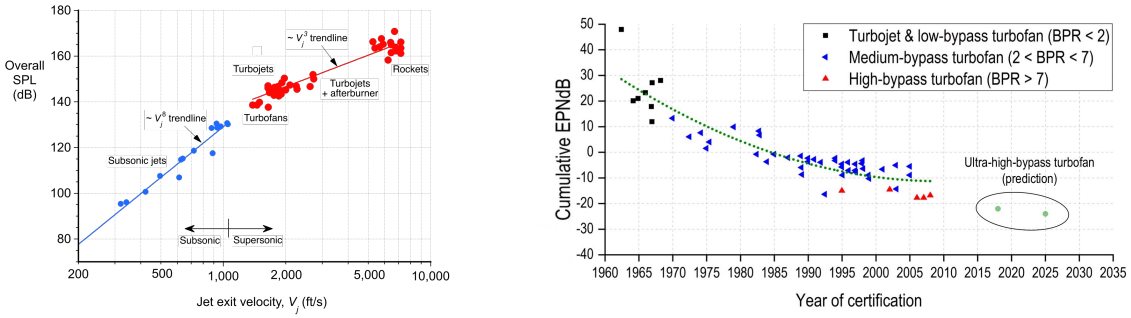

(a) Power Law for Noise Jet Engines [43]

(b) Noise emission over different years [64]

Figure 1.5: Historical evolution of engine noise [EPNdB = effective perceived noise level in decibels]

the "Chevron technique" [47] in order to reduce jet noise. This technique, which consists of using serrations on the engine nozzle, has been studied over time by many researchers [10, 65]. These studies identified the main noise reduction mechanisms as the energetic inhibition of ring-like coherent structures and improved entrainment. Therefore, these studies have enabled the equipment of large commercial aircrafts with this technique, as can be seen in Figure 1.6, which shows a "Boeing 737-8200 MAX" operated by Ryanair:

Figure 1.6: Boeing 737-8200 MAX

Fan noise, instead, according to Filippone [28], dominates most flight conditions and is extremely complex to predict due to its strong relationship with the tip Mach number, fan compression ratio, and rotor-stator spacing [18]. The fan stage consists of two main elements: the rotating fan (rotor) and the downstream outlet-guide vanes (OGVs/stator), which are used to improve the aerodynamic efficiency of the turbofan by recovering the swirl in the fan wake.

The noise generated by the interaction between the wake left by the rotor and the OGV vanes has a significant acoustic impact, especially at low Mach numbers. According to Teruna [64], this interaction noise has a tonal component induced by the periodic part of the impinging wake and a broadband component related to the various scales of turbulence in fan wake. Moreover, according to Paruchuri [53], there are other forms of broadband noise related to the rotor: specifically, the interaction of boundary layer vortices flowing over the rotor with the trailing edge , and the interaction between tip vortices and the boundary layer of the engine inlet. All this information is summarized in Figure 1.7, where the distinction between interaction noise (usually referred to as Airfoil–Gust Interaction (AGI) noise) and self-noise is reported. Interaction noise, according to Turner and Kim [69], turns out to be the sum of multiple components: a primary component known as “leading edge vortical scattering” (LEVS) and “acoustic backscattering” (ABS), which together with “trailing edge vortical scattering” (TEVS) make up the secondary noise component. "Self-noise," instead, is the noise arising from the interaction between an airfoil and its own turbulent boundary layer, assuming a smooth non-turbulent inflow [5]. According to Paruchuri [53], this component tends to play a marginal role for thin airfoils, such as the OGVs which are 5% thick

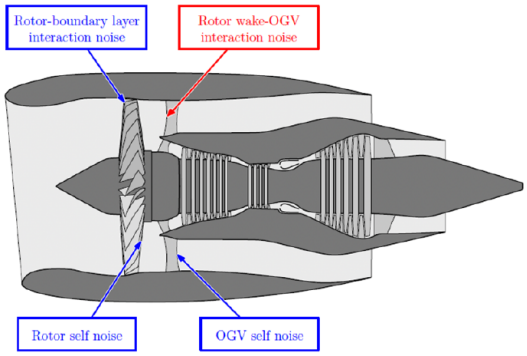

Figure 1.7: Noise generation mechanism of the interaction noise between the rotor wakes and the stator [53]

The study of AGI noise on OGVs has been extensively conducted with the goal of identifying technological solutions to reduce acoustic emissions. The application of undulations (serrations) to the leading edge (WLE) has proven capable, as explained by Paruchuri et al. [54], of reducing acoustic emissions by up to 18 dB at specific frequencies, although a precise ratio between the WLE wavelength and the incident gust is required, as noted by Paruchuri [53]. Numerous numerical studies, such as the one by Kim et al. [41], have attributed these reductions to phase-shifting phenomena—or equivalently, a delay in the activation of acoustic sources located between peaks and valleys—leading to a subsequent weakening of the aerodynamic loads. However, in addition to structural weakening, Narayanan et al. [46] highlighted how the aerodynamic performance of a flat plate with a serrated leading edge is significantly compromised. While drag and boundary layer separation might, under certain conditions, even benefit from the increased momentum transport induced by the vortices generated by the serrations, the lift coefficient is sharply reduced, as pointed out by Paruchuri [53]. Therefore, the potential advantages of employing porous treatments remain the subject of extensive ongoing research.

Chapter 2

Literature review

> *"La vida es corta, perdona rápido, no discutas por tonterías, besa lento, ama de verdad, cela un poco, no mucho, solo un poco, ríete sin control y nunca dejes de sonreír por mas extraño que sea el motivo. Puede ser que la vida no sea la fiesta que esperabas, pero mientras estés aquí, tienes que bailar."*
>
> — Dante Gebel

The following chapter aims to present some of the main results obtained in the study of acoustic reduction through porous media, focusing on the physical mechanisms considered fundamental to noise reduction.

While on the one hand numerical and experimental evidence shows that porous materials are the key technology for acoustic reduction [76, 30], on the other hand, the complex analysis of fluid dynamics in these materials has so far left the underlying mechanisms unclear, as highlighted by Palleja-Cabre et al. [52]. This uncertainty is due to the large number of parameters influencing the phenomenon, most notably the airfoil thickness. In an attempt to understand how a thick NACA airfoil with a porous leading edge (LE) could alter the impinging vortex shedding (generated downstream of a cylinder), Zamponi et al. [76] identified an acoustic reduction at low frequencies and an increase at high frequencies due to surface roughness. The noise reduction was associated with a less efficient sound conversion attributed to a less pronounced distortion of the fluid near the airfoil, caused by permeability at the leading edge [74], and decreased vertical velocity fluctuations, leading to a reduction in surface pressure fluctuations [75]. Specifically, this latter mechanism is caused by the penetration of the flow into the porous material—and thus the lack of complete stagnation at the leading edge—which prevents an increase in the local angle of attack and the consequent shift of intensity from streamwise to upwash fluctuations, which are instead dissipated.

Both the mechanism of turbulent kinetic energy dissipation and the reduction in surface pressure fluctuations following a displacement of incident turbulent structures have also been experimentally confirmed by Geyer et al. [30], who identified acoustic reductions at low-to-medium frequencies of up to 8 dB. In addition to the aforementioned reduction mechanism, an increase in the boundary layer thickness is identified, leading to an apparent thickening of the leading edge capable of reducing interaction acoustic emission.

Chaitanya et al. [9] compared the noise-generation mechanisms in fully and partially porous flat plates (hereafter referred to as FP and PP, respectively), demonstrating that, in addition to the dissipative mechanism, additional mechanisms play a more significant role and are better suited to the thin-profile configurations characteristic of components, such as OGVs. Firstly, they identified acoustic sources in two compact pressure jumps generated at the leading edge and at the end of the porous area of length l, present only in the PP study, and the pressure jump distributed over the entire porous area, present in both PP and FP. Secondly, two acoustic reduction mechanisms were identified. The first one was the "cut-off " of the distributed source (present in both FP and PP configurations), generated by an advection velocity of the pressure jump lower than the speed of sound, which presented reduction peaks at integer values n of the Strouhal number calculated as fl/U_c, where U_c represents the advection velocity assumed to be $0.7 \cdot U_\infty$. The second one was

the destructive interference between compact sources (present only in the PP configuration), which presented reduction peaks at $fl/U_c = n - 1/2$.
The cut-off mechanism, also cited by Kim et al. [41] in their study of serrations, is strictly linked to the concept of evanescent modes—i.e., subcritical waves incapable of propagating into the far field. Destructive interference, on the other hand, is generated by phase delay, which refers to the different generation times of the sound waves resulting from the varying displacement of the sources in the streamwise direction.

Since the presence of porosity on the leading edge can be detrimental to the aerodynamic performance of the airfoil, leading to a reduction in lift and a drag increase of approximately 30% [51], the application of porosity has been studied by extending it downstream of the leading edge; indeed, Chaitanya et al. [8] and Ocker et al. [50] demonstrate how aerodynamic performance improves with this technique rather the leading-edge perforation.

Motivated by the possibility of exploiting the potential aerodynamic benefits that such a configuration could entail, Palleja-Cabre et al. [52] conducted an experimental study of turbulent flow over a flat plate with a porous extension l positioned up to a distance l_d from the LE. A step forward in understanding the mechanisms triggered by downstream porosity was achieved with this study, as he identified the phase inversion of π ($e^{i\pi}$) between the compact source on the leading edge and those on the porous zone as a new additional destructive interference mechanism. The experimental analysis conducted highlighted both the presence of acoustic reduction peaks at $fl_d/U_c = n$ and the strong similarity, in terms of acoustic spectra, between a plate with downstream porosity and two flat plates in a tandem configuration.

The phase inversion described above has been attributed to possible secondary vorticity with a direction of rotation opposite to that of the primary vortex incident on the leading edge. However, this study was based on two assumptions: the imposition of equal intensity of compact sources, which allowed the shape of the spectra to be evaluated but not the absolute values, and that a frozen advection of secondary vorticity was taken into account neglecting any non-linear phenomena.

The importance of non-linear phenomena was first examined by several theoretical and numerical studies, demonstrating that if a linear model is considered, part of the overall noise can vanish, accompanied by alterations in the lift profiles. The linearity assumptions, which are in fact extremely difficult to achieve, would require that vortices positioned very far from the flat plate and of low intensity induce a velocity much lower than the mean freestream velocity [33]. According to Turner and Kim [69], non-linear mechanisms govern the interaction and the non-linear growth of boundary layer instabilities—whose frequency exactly matches the peak of the trailing-edge noise—responsible for vortex stretching and tilting [68], leading to the fragmentation of turbulent structures from large to small scales as the flow progresses from the leading edge to the trailing edge.

Theoretical studies such as the one carried out by Abou-Hussein et al. [1] have partly demonstrated the importance of a non-linear interaction model to visualize acoustic sources. Supporting this, Priddin et al. [56] investigated the acoustic scattering on a flat plate in tandem using Helmholtz's linear equation. Their study did not reveal distinct peaks in acoustic reduction but reported only an overall average decrease. More recently, Feng and Ye [25] conducted an experimental study using tomographic particle image velocimetry (tomo-PIV) to understand the physical mechanisms governing flow behavior on porous plates, identifying numerous alterations in fluid structures due to porous-induced Kelvin-Helmholtz waves. Since skin friction is an effect induced by coherent structures [45], any alteration of the fluid structures also alters the skin friction, in accordance with the critical value of permeability normal to the wall defined by Feng and Ye [25]. Beyond this value (or similarly, for K_{xy}/K_y ratios lower than 1, where K_y is the normal permeability of the wall), an increase in skin friction occurs. This increase is confirmed and justified by [4], who explains how an increase in wall-normal porosity triggers the growth of Kelvin-Helmholtz waves. This is followed by an increase in vorticity and a subsequent intense exchange of momentum through the pores, which leads to an increase in the Reynolds stress tensor and, consequently, in skin friction.

At the same time, in [4], the disappearance of low/high-speed streaks in the streamwise direction (and the reduction of the RMS peak of streamwise fluctuations) was highlighted as permeability increased, quantified by Re_K, and as wall-blocking was reduced. While on one hand the mutual dependence between spanwise coherent structures and Kelvin-Helmholtz waves is known, on the other hand, it was necessary to decouple the contribution of KH waves from other structures.
Therefore, in [42], a parametric study was carried out by acting on the dimensions of the com-

putational domain in order to separate the contribution between spanwise rollers and near-wall turbulence motion (streaks and longitudinal vortices). What emerged is that wall-normal permeability is necessary for the development of spanwise rollers, which in turn are necessary for an increase in skin friction and turbulent intensity within the pores themselves, in agreement also with Gómez-de Segura and García-Mayoral [32], where an ordinary reduction in friction was reported as long as a critical value of permeability normal to the wall was not exceeded. Beyond this value, spanwise-coherent structures generated by Kelvin-Helmholtz instabilities are observed, which lead to an increase in skin friction.
This latter aspect is also validated by the experimental work reported in [25] where, by analyzing the mean flow quantities, a clear downwash effect within the pores emerged.
Although some aspects remain highly debated, it is ultimately clear that Kelvin-Helmholtz waves, induced by momentum transport through the pores, cause an alteration of the boundary layer.

This thesis work investigates the behavior of a turbulent flow over a flat plate with anisotropic downstream porosity, using a Very Large Eddy Simulation (VLES) conducted with the Lattice-Boltzmann Method solver, Powerflow. The porosity, located downstream of the leading edge, consists of eight rows of appropriately spaced cylindrical holes. By assuming the validity of Rayleigh's criterion and through visual inspection of the spanwise vorticity field, the presence of KH waves and their subsequent fragmentation was confirmed. This fluid-dynamic structure, induced by the pores, was found to be associated with a reduction in the mean velocity and, consequently, the convection velocity; then confirmed by the analysis of the convection ridge. This analysis revealed the presence of a first near-field acoustic cone with lower energy compared to a second one generated at significantly lower acoustic propagation speeds, suggesting a mechanism of cut-off or evanescent modes. This aspect, will require further investigation. Following a decomposition between hydrodynamics and acoustics in the near field, a study was conducted on the phase shift between the acoustic sources at the leading edge and those within the porous zone, which appears to exhibit phase opposition at integer Strouhal numbers similarly to acoustic reduction observed by Palleja-Cabre et al. [52].

Chapter 3

Mathematical background

"...and you're singing the song thinking this is the life and you wake up in the morning and your head feels twice the size where you gonna go, where you gonna go, where you gonna sleep tonight?..."

— Amy MacDonald

In this chapter, a brief introduction to the Lattice Boltzmann method used in the PowerFlow solver is provided, clarifying its connection with the Navier–Stokes equations and the use of the immersed boundary method (IBM) approach, which differs from classical body-fitted (BF) methods. Finally, some information will be given regarding the concept of order of accuracy as applied to IBM.

3.1 Brief notes on the link between the Inviscid Navier-Stokes equations and the Boltzmann equation

In recent years, the Lattice-Boltzmann Method (LBM) has been developed as an alternative to conventional Navier-Stokes computational fluid dynamics (NS-CFD) methods, such as the finite volume and finite difference methods. In fact, as reported in the PhD thesis of Chin [14], under certain hypotheses, the Navier-Stokes equations (which describe the macroscopic world) can be derived from the Boltzmann equations. The latter describe a microscopic world in which particles move on a lattice, interacting with each other through collisions and propagation.
The equations of motion describing the microscopic world treat the fluid as a collection of small point particles (at position $\mathbf{x}$ with momentum $\mathbf{p}$) characterized by a specific number of degrees of freedom. These particles are subjected to external forces (such as gravity) and interact with one another through force fields, such as electromagnetic forces.
This motion can be described via the Hamiltonian, defined as the sum of kinetic and potential energy:

$$H = T + V = \sum_{i=1}^{N} \frac{p_i^2}{2m} + \sum_{i=1}^{N} \sum_{j>i} \Phi_{ij} \tag{3.1}$$

where $\Phi_{ij} = \Phi(|\mathbf{x}_i - \mathbf{x}_j|)$ represents the interaction potential between particles at $\mathbf{x}_i$ and $\mathbf{x}_j$. This potential is a function of the magnitude of the relative distance. Note that the interaction of particle i with j is identical to that of j with i. [1]
One of the triumphs of modern kinetic theory has been demonstrating that it is possible to transition from a microscopic Hamiltonian description to the macroscopic Navier-Stokes equations. This is achieved by systematically integrating out irrelevant degrees of freedom (DOFs) from the $6N$ DOFs in Equation 3.1 where N is the particles number.
The transition from the Hamiltonian description to the Navier-Stokes equations is achieved via the Liouville equation, which provides a probabilistic interpretation of the motion. When appropriately treated, Liouville equation leads to the Boltzmann equation and, ultimately, to the Navier-Stokes

[1] This symmetry is reflected in the summation indices $j > i$ to avoid double-counting.

equations.
The Liouville equation describes a system of N particles using an "N-particle distribution function" (Eq. 3.2), which represents the probability density of finding particle 1 with momentum $\mathbf{p}_1$ at position $\mathbf{x}_1$, particle 2 with momentum $\mathbf{p}_2$ at $\mathbf{x}_2$, and so on:

$$\psi\left(\mathbf{x}_1, \mathbf{p}_1, \ldots, \mathbf{x}_N, \mathbf{p}_N; t\right) \tag{3.2}$$

Hereinafter, $\mathbf{z} = (\mathbf{x}, \mathbf{p})$.
The probability density ψ is then transported, with advection speed $\dot{\mathbf{z}}$, via a simple advection equation since Ψ is conserved as indicated in the following equation 3.3:

$$\left(\frac{\partial}{\partial t} + \sum_i \dot{\mathbf{z}}_i \cdot \frac{\partial}{\partial \mathbf{z}_i}\right) \psi = 0 \tag{3.3}$$

The second term of the equation 3.3 presents a spatial derivative applied to the ψ which can be more compactly rewritten using *Liuvillan* in the following way:

$$\mathcal{L}_N\left(\mathbf{z}_1, \ldots, \mathbf{z}_N\right) \doteq \sum_{i=1}^{N} \frac{1}{m} \mathbf{p}_i \cdot \frac{\partial}{\partial \mathbf{x}_i} + \sum_{i=1}^{N} \sum_{j>i} \mathbf{K}_{ij} \cdot \left(\frac{\partial}{\partial \mathbf{p}_i} - \frac{\partial}{\partial \mathbf{p}_j}\right),$$

where the force $\mathbf{K}_{ij}$ exerted on particle i by particle j is

$$\mathbf{K}_{ij} \doteq -\frac{\partial}{\partial \mathbf{x}_i} \Phi\left(|\mathbf{x}_i - \mathbf{x}_j|\right).$$

We then arrive at the well-known Liuville equation:

$$\left(\partial_t + \mathcal{L}\right) \psi = 0 \tag{3.4}$$

As mentioned above, to arrive at the Navier-Stokes equations it is necessary to reduce the number of degrees of freedom. This is done via an integration process that leads to the definition of a cascade of equations known as BBGKY (Bogoljubov-Born-Green-Kirkwood-Yvon).
These equations take the form $f_1(z_1, t), f_2(z_1, z_2, t), \ldots, f_n(z_1, \ldots, z_n, t)$ and represent probability distributions similar to ψ. However, they differ in their normalization: when properly integrated, f_i do not sum to 1, but rather to N (the number of particles and/or degrees of freedom (DOFs)).
Unlike f_1, which describes the single-particle probability distribution in phase space, the functions $f_2, f_3, \ldots, f_n$ measure the correlation levels among $2, 3, \ldots, n$ particles. Indeed, they depend on the coordinates $(\mathbf{z}_1, \mathbf{z}_2), (\mathbf{z}_1, \mathbf{z}_2, \mathbf{z}_3), \ldots, (\mathbf{z}_1, \ldots, \mathbf{z}_n)$, respectively.
In other words, these functions describe the correlation probabilities among $2, 3, \ldots, n$ particles (where $n < N$). Specifically, in transitioning from f_n to f_{n+1}, an additional degree of freedom is considered, while the remaining ones are integrated out.
Integration serves as a way to average out, and thus reduce, the $N - n$ degrees of freedom of the system as described in equation 3.5

$$f_1\left(\mathbf{x}_1', \mathbf{p}_1', t\right) = f_1\left(\mathbf{z}_1', t\right) \doteq N \int \psi\left(\mathbf{z}_1', \mathbf{z}_2 \ldots \mathbf{z}_N\right) \mathrm{d}\mathbf{z}_2 \cdots \mathrm{d}\mathbf{z}_N \tag{3.5}$$

Since f_1 is evaluated, ψ is integrated by z_2 to z_N. Having said these premises, it is possible to reduce the 6N degrees of freedom of the system by integrating to have only n<N.
Following this approach, the N degrees of freedom of the Liouville equation (3.4) can be reduced to n; therefore, the integration is carried out from $n+1$ up to N, as shown in Eq. 3.6 and Eq. 3.7:

$$\int \left(\frac{\partial}{\partial t} + \mathcal{L}_n\right) \psi \mathrm{d}\mathbf{z}_{n+1} \ldots \mathrm{d}\mathbf{z}_N = -\int \sum_{i=1}^{n} \sum_{j=n+1}^{N} \mathbf{K}_{ij} \left(\frac{\partial}{\partial \mathbf{p}_i} - \frac{\partial}{\partial \mathbf{p}_j}\right) \psi \mathrm{d}\mathbf{z}_{n+1} \ldots \mathrm{d}\mathbf{z}_N \tag{3.6}$$

Some further algebra to simplify and recast this in terms of distribution functions yields the famous chain of equations

$$\left(\frac{\partial}{\partial t} + \mathcal{L}_n\right) f_n = -\sum_{i=1}^{n} \int \mathbf{K}_{i,n+1} \cdot \frac{\partial}{\partial \mathbf{p}_i} f_{n+1} \, \mathrm{d}\mathbf{z}_{n+1} \tag{3.7}$$

Examining the hierarchy in Equation 3.7, we observe that it is an no-closed problem, as determining f_n requires knowledge of f_{n+1}. It is therefore necessary to introduce approximations to close the system, which leads to the Boltzmann equation.
Starting from the first level of the BBGKY hierarchy ($n = 1$):

$$\left(\frac{\partial}{\partial t} + \frac{1}{m}\mathbf{p}_1 \cdot \frac{\partial}{\partial \mathbf{x}_1}\right) f_1 = -\int \mathbf{K}_{12} \cdot \frac{\partial}{\partial \mathbf{p}_1} f_2 \, \mathrm{d}\mathbf{z}_2 \tag{3.8}$$

and seeking a way to close the problem, we define the gas rarefaction level using the parameter λ. This allows us to expand the distribution functions as:

$$\begin{aligned} f_1 &= \lambda f_1^0 + \lambda^2 f_1^1 + \lambda^3 f_1^2 + \dots \\ f_2 &= 0 + \lambda^2 f_2^0 + \lambda^3 f_2^1 + \dots \\ f_3 &= 0 + 0 + \lambda^3 f_3^1 + \dots \end{aligned} \tag{3.9}$$

where it can be observed that f_1, being indicative of density, is linear in λ (which relates to the number of particles in a given volume), while $f_2 \dots f_n$ are of higher order in λ.
Substituting these expansions into the first BBGKY equation ($BBGKY_1$), it is essential to maintain consistency in the order of λ for both f_1 and f_2. In other words, if f_1 is expanded only to the leading order (λ), then f_2 vanishes, as shown in the expansion scheme 3.9. In this case, the first BBGKY equation describes the transport of non-colliding particles, as the interaction term on the right-hand side disappears.
Conversely, if f_1 is expanded to the second order (λ^2), the first term of f_2 also appears. In this scenario, the right-hand side retains the interaction (collision) term, as seen below: [2]

$$\left(\frac{\partial}{\partial t} + \frac{1}{m}\mathbf{p}_1 \cdot \frac{\partial}{\partial \mathbf{x}_1}\right) f_1^1 = -\int \mathbf{K}_{12} \cdot \frac{\partial}{\partial \mathbf{p}_1} f_2^0 \, \mathrm{d}\mathbf{z}_2 \tag{3.10}$$

However, the problem remains no-closed; therefore, several necessary approximations are reported below:

1. The following postulate is utilized:

   Theorem 1 (Postulate of Molecular Chaos (Boltzmann's *Stosszahlansatz*))**.** *Any two particles in the system are assumed to be uncorrelated before and after their brief collision. Mathematically, this is equivalent to neglecting the two-particle correlation function and expressing the two-particle distribution function as the product of individual one-particle distribution functions:*

   $$\boxed{f_2(\mathbf{z}_1, \mathbf{z}_2) \simeq f_1(\mathbf{z}_1) f_1(\mathbf{z}_2)}$$

2. It is assumed that the single-particle distribution functions, f_1, exhibit negligible spatial variation over the range of the intermolecular force. This assumption effectively refines the approximation from the aforementioned theorem by localizing the interaction.

3. Following from point 2, the force exchanged between two particles, $\mathbf{K}_{ij}$, is more conveniently expressed in terms of the relative momentum $\mathbf{g} = (\mathbf{p}_1 - \mathbf{p}_2)/m$.

4. Consequently, the distribution functions can be re-evaluated at a common reference position, $\mathbf{x}$, leading to:

   $$\begin{aligned} &f_1(\mathbf{z}_1) = f_1(\mathbf{x}_1, \mathbf{p}_1) \to f_1(\mathbf{x}, \mathbf{p}_1) \\ &f_1(\mathbf{z}_2) = f_1(\mathbf{x}_2, \mathbf{p}_2) \to f_1(\mathbf{x}, \mathbf{p}_2) \\ &\text{with } \mathbf{x} \text{ representing the local interaction point.} \end{aligned} \tag{3.11}$$

5. Based on the definitions in point 3, we define the particle velocities (at the mesoscale level) as:

   $$\mathbf{c}_i = \frac{\mathbf{p}_i}{m} \tag{3.12}$$

[2] Note that the term $(f_1)^0$ is absent in this equation; it is identically zero based on the first-order expansion in λ described previously.

Thanks to this assumption, we obtain:

$$\left(\frac{\partial}{\partial t}+\frac{1}{m}\mathbf{p}_1\cdot\frac{\partial}{\partial \mathbf{x}_1}\right)f_1=\int \mathbf{g}\cdot\frac{\partial}{\partial \mathbf{r}}\left[f_1\left(\mathbf{r},\mathbf{p}_1\right)f_1\left(\mathbf{r},\mathbf{p}_2\right)\right]\mathrm{d}\mathbf{z}_2 \tag{3.13}$$

which, when compacted (using Einstein notation), becomes the Boltzmann Equation:

$$\left(\partial_t+c_\alpha\partial_\alpha\right)f=\Omega[f] \tag{3.14}$$

From this, it follows that:

1. This equation is in a closed form, as it depends on only one distribution function.

2. It describes the fluid at a mesoscopic level—an intermediate scale between the microscopic and macroscopic.

In fact, the macroscopic quantities of a fluid are obtained by integrating the mesoscopic variables:

$$\begin{aligned}\rho&=m\int f\ \mathrm{d}\mathbf{c}\\ \rho\mathbf{u}&=m\int f\mathbf{c}\ \mathrm{d}\mathbf{c}\\ E&=\frac{m}{2}\int fc^2\ \mathrm{d}\mathbf{c}\end{aligned} \tag{3.15}$$

3. This equation is time-asymmetric; specifically, it is temporally irreversible. This implies a preferential direction for the "arrow of time," where distribution functions tend toward an equilibrium state known as the Maxwell-Boltzmann distribution:

$$\bar{f}=\frac{\rho}{(2\pi\theta)^{d/2}}\exp\left(-\frac{(\mathbf{c}-\mathbf{u})^2}{2\theta}\right) \tag{3.16}$$

Consequently, the Boltzmann equation can be rearranged by modeling the collision operator $\Omega[f]$—which represents particle interactions and correlations—using a relaxation approximation. This leads to the BGK equation[3]:

$$\partial_t f+c_\alpha\partial_\alpha f=-\frac{1}{\tau}(f-\bar{f}) \tag{3.17}$$

In this framework, collisions cause the distribution function to relax toward equilibrium ($f\longrightarrow\bar{f}$) over a characteristic relaxation time τ.

To derive the continuity equation from the BGK model, the Chapman-Enskog expansion is required. This involves expanding the time and space derivatives, as well as the distribution functions, in a manner similar to Eq. 3.9. Integrating over the particle velocity space c allows for the transition from the mesoscale to the macroscale (Navier-Stokes equations).

Below is a qualitative derivation demonstrating how the BGK model recovers the fundamental equations of fluid dynamics:

$$\begin{aligned}&\int\partial_t f\mathrm{d}\mathbf{c}+\int c_\alpha\partial_\alpha f\mathrm{d}\mathbf{c}=\int-\frac{1}{\tau}(f-\bar{f})\mathrm{d}\mathbf{c}\\ &\partial_t\underbrace{\int f\mathrm{d}\mathbf{c}}_{\rho}+\partial_\alpha\underbrace{\int c_\alpha f\mathrm{d}\mathbf{c}}_{\rho u_\alpha}=-\frac{1}{\tau}\underbrace{\int(f-\bar{f})\mathrm{d}\mathbf{c}}_{=0}\\ &\boxed{\partial_t\rho+\partial_\alpha\rho u_\alpha=0}\end{aligned} \tag{3.18}$$

[3]Bhatnagar, Gross, and Krook

3.2 Brief Notes on Numerical Approaches and the Immersed Boundary Method

The analytical resolution of the equations previously described (Hamilton's equations and the BKI equation) is generally unfeasible; therefore, numerical approaches are employed. Of particular interest is the Lattice Boltzmann Method (LBM), which evolved from Lattice Gas Automata (LGA). A lattice gas consists of a collection of particles constrained to the sites of a regular lattice. Every point $\mathbf{r}$ on the lattice is associated with a set of vectors $\mathbf{c}_i$ that connect it to its nearest neighbors; the velocity of each fluid particle is restricted to one of these vectors. During each timestep of the algorithm, particles move to adjacent points according to their velocity vectors; they may collide with other particles if they occupy the same site, as illustrated in Figure 3.1.

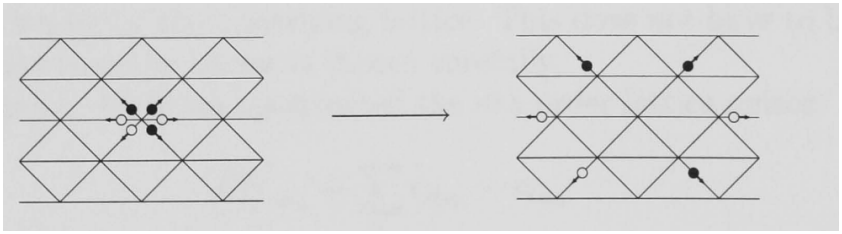

(a) Advection step in Lattice Gas Automata

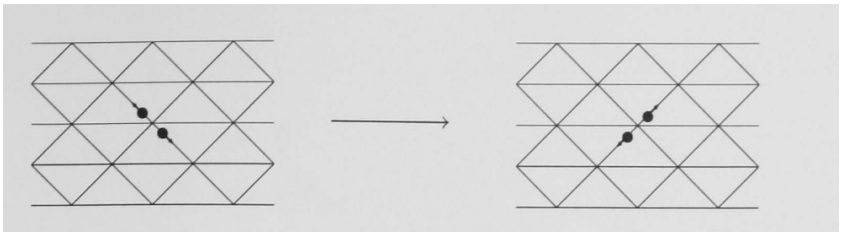

(b) Collision step in Lattice Gas Automata

Figure 3.1: Steps in LGA [Chin [14]]

It is reasonable to consider the advection phase as being solved by setting the collision operator to zero, while the collision (specifically the post-collision phase) involves a non-zero collision operator.

The discrete formulation of the Boltzmann equation 4.1 is given by:

$$f_i\left(\mathbf{r}+\mathbf{c}_i, t+1\right)-f_i(\mathbf{r}, t)=\Omega_i(\mathbf{r}, t) \tag{3.19}$$

This equation is appropriately modeled (using the Chapman-Enskog expansion and the averaging processes described in 3.15) to derive the macroscopic formulation, and consequently, the Navier-Stokes (NS) equations. Historically, high computational costs arose from the necessity of integrating these quantities while simultaneously solving the distribution functions. LBM circumvents this by evaluating fluid-dynamic quantities only after calculating the distribution functions [14].

However, determining the most effective way to estimate the collision operator is crucial. Some approaches attempted to preserve the "collision character" by rewriting Ω using polynomial forms involving distributions of neighboring points with a wider stencil; however, these proved difficult to implement in three dimensions. Others, such as Higuera et al. [36], utilized linearization processes of the collision operator with non-equilibrium distribution functions. The most effective solution was provided by the BGK approximation, in analogy to the continuous formulation of the Boltzmann equation, where:

$$\Omega \simeq \frac{f^{(\mathrm{eq})}-f}{\tau} \tag{3.20}$$

The equilibrium distribution f_{eq} can take various forms but remains a function of macroscopic quantities. The primary advantages of BGK over LGA include a significant reduction in numerical noise and greater ease of implementation, though this comes at the cost of losing the unconditional stability characteristic of LGA [14].

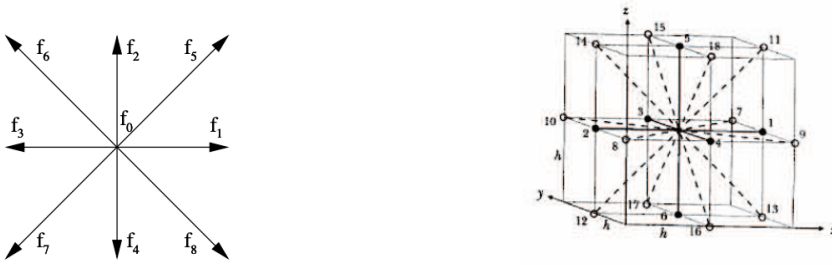

(a) D2Q9 (b) D3Q19 (Used in PowerFLOW)

Figure 3.2: Set of possible particle velocities within the lattice [35]

As previously explained, particles can only occupy discrete positions within the lattice, with velocities limited to a specific number of directions and magnitudes based on the chosen lattice type. These are defined as $DkQb$, as shown in Figure Figure 3.2, where k represents the number of dimensions and b the number of velocity vectors. The choice of lattice directly defines the form of f_{eq}. The imposition of BC occurs through macroscopic quantities that subsequently they are "translated" in terms of distribution functions.
The most suitable discretization technique for the LBM is the Immersed Boundary Method (IBM), as illustrated in Figure 3.3.

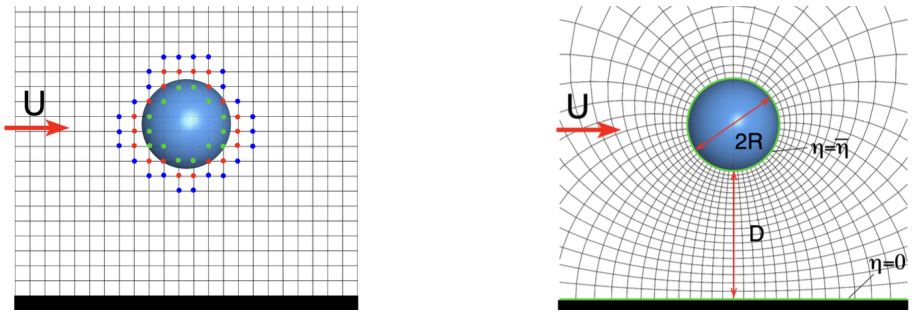

(a) Immersed Boundary Method (b) Body-fitted grid

Figure 3.3: Different meshing methods [60]

Immersed Boundary Methods employ regular grids (predominantly Cartesian) and handle irregular wall boundaries by partially blocking the cells intersected by the surfaces. The rationale for using IBM is multifaceted and addresses several weaknesses inherent in traditional body-fitted meshes [60]:

1. The translation of surfaces from CAD to CFD is non-trivial for complex geometries;

2. Grid generation is not highly time-consuming and not requires specialized expertise;

3. IBM is considered more flexible than body-fitted grids for studying flows around moving or deforming bodies according to Ferziger and Perić [26]. For instance, a solution for moving surfaces proposed by R.Verzicco [60] involves keeping the body stationary while applying variable forces to the velocity field to replicate the effects of the body's motion;

4. elements can be refined or coarsened without altering adjacent elements [35].

   In other words, refinement zones are created by splitting voxels into smaller sub-units while leaving the surrounding external cells unchanged. To illustrate this, consider Figure 3.4: if cells "2" are adjacent to a wall and require refinement, each cell "2" is split into two parts to obtain cells "3". Due to the high regularity of the mesh, this process does not alter the grid structure containing the larger cells.

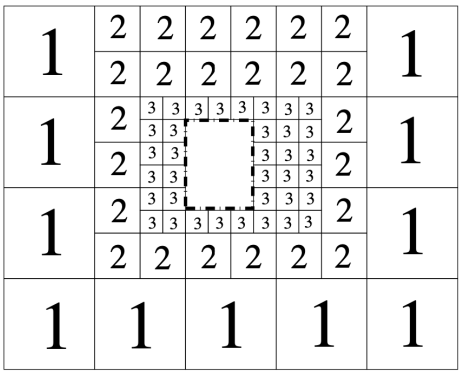

Figure 3.4: Refinement logic with IBM [35]

However, the primary challenge lies in imposing accurate wall boundary conditions. If walls are in motion the identification of cut cells and cells outside the computational domain must be performed at every timestep.

3.3 Brief notes on Accuracy order in LBM

The purpose of this chapter is not to provide a formal and exhaustive description of these concepts; however, it is worth noting that:

- The order of accuracy is directly linked to the truncation error and, consequently, to the discretization error.
- The discretization error (ED) arises from replacing a continuous problem with a discrete one. It is defined as the difference between the exact solution of the exact differential problem ($EDDP_{ex}$) and the exact solution of the relative discrete formulation (EDF_{ex}), assuming both are unaffected by round-off errors:

$$(EDDP)_{ex} - (EDF)_{ex} = ED = ET + ECC \tag{3.21}$$

  Alternatively, it can be expressed as:

$$\mathscr{L}(\Phi) = L_{\Delta x}(\Phi) + \tau_{\Delta x} = 0 \tag{3.22}$$

  where Φ is the exact solution of the EDDP but not of the discrete problem.

- The truncation error, conversely, relates to the solution itself; it is the difference between the solution $\phi_{\Delta x}$, which satisfies the algebraic/numerical problem ($L_{\Delta x}(\phi_{\Delta x}) = 0$), and the exact solution Φ, which satisfies the $EDDP$ ($\mathscr{L}(\Phi) = 0$).

It is evident that the truncation error drives the discretization error. By expanding the discretization error, the truncation error can be approximated as:

$$\varepsilon^d_{\Delta x} \approx \alpha \Delta x^p + H \tag{3.23}$$

Unlike Finite Difference (FD) or Finite Volume (FV) methods, where the estimation of the order of accuracy is well-established and depends almost entirely on the numerical scheme employed, this is no longer the case for the LBM. A vast number of factors influence the overall accuracy of the method; consequently, even under identical conditions, simulations of different physical problems may exhibit varying degrees of precision.

To investigate this phenomenon, Zagvozdina and Burovski [73] implemented various types of spatial grids, boundary conditions (such as link-wise bounce-back and wet-node bounce-back methods[4]), and equilibrium distribution functions *(using 1st and 2nd order expansions)*. This demonstrated that accuracy is strongly influenced by a multitude of parameters. Their results showed

[4]Link-wise bounce-back represents simple particle rebound. The wet-node bounce-back method is more complex and precise, as it also accounts for the tangential components of wall momentum, which are neglected in the former case.

that changing the boundary conditions (BCs) or the order of expansion did not significantly alter convergence. However, Francesca Tosi [29] indicates that "Link-wise bounce-back" boundary conditions generally provide first-order accuracy, which increases to second-order only if the wall bisects the voxel perfectly.

This confirms that the overall accuracy is determined by the interplay of all parameters rather than a single factor. Given the difficulty in accurately quantifying the order of accuracy, an approach suggested by Roache [59] is adopted. This method is based on the results of three simulations of the same problem performed at different refinement levels:

$$p = \frac{\ln\left(\frac{f_3 - f_2}{f_2 - f_1}\right)}{\ln(r)} \tag{3.24}$$

where:

- f_i is the parameter used in the convergence analysis;
- r is the refinement ratio, which defines the rate at which the mesh is refined.

Chapter 4

Methodology

"E' l'unione delle singole armonie a creare una variazione di intensità sonora: non c'è bisogno che suoniate forte"

— *M° Michele Marzella*

In this chapter, the geometrical and numerical setup is described, providing all the necessary details to estimate the parameters required for the simulation.

4.1 Flow Solver

The commercial software Simulia PowerFLOW 6-2021 has been used to compute the flow field. The software is based on lattice-Boltzmann Method (LBM) and employs the "immersed boundary method" technique, which offers significant advantages with respect to traditional body-fitted methods [60, 27]. The LBM model [14] describes a fluid at the mesoscale level through a process of advection and collision between particles that alters the particle distribution function. This spatial and temporal alteration is described by Boltzmann's equation in the form:

$$(\partial_t + c_\alpha \partial_\alpha) f = \Omega[f] \tag{4.1}$$

f represents the distribution of n particles and takes into account the correlations between them, c_α is the particle speed and Ω is the collision operator. Eq. 4.1, unlike the equations used in its proof, is time-asymmetric, which means that it cannot be reversed in time [14]. There is thus a single temporal direction and thus a single time scale τ during which equilibrium conditions tend to be reached [11]. This means that the Boltzmann equation can be rearranged such that the collision operator (which indicates the forces exchanged between two particles and the levels of probable correlation between multiple particles involved in the collision) $\Omega[f]$ can be expressed as

$$\partial_t f + c_\alpha \partial_\alpha f = -\frac{1}{\tau}(f - \bar{f}). \tag{4.2}$$

In other words, during the collision there is a relaxation of the distribution functions (f hence tends to $\bar{f}$) which occurs in a time τ. This is the Bhatnagar, Gross, and Krook (BGK) equation. The discrete formulation of the BGK equation is the following

$$f_i\left(\mathbf{r} + \mathbf{c}_i, t + 1\right) - f_i(\mathbf{r}, t) = \Omega_i(\mathbf{r}, t), \tag{4.3}$$

which describes a process of advection (zero collision operator) and collision (non-zero collision operator) of particles moving on a 3D lattice in 19 precise directions (D3Q19). The transition from Eq. 4.3, which analyzes the mesoscale, to the NS equation (macroscale) is made using the 3^{rd} order Chapman-Enskog expansion. This consists of expanding both the time derivatives and the probability functions f using the Knudsen number as the expansion coefficient [14]. Regarding the collision operator, the most commonly used formulation is the one that approximates the continuous BGK formulation like in Eq. 4.2, with expansion of f^{eq} to the second order [12]:

$$f_i^{\text{eq}} = \rho\omega_i \left[1 + \frac{\boldsymbol{V}_i \boldsymbol{u}}{\mathrm{a_s^2}} + \frac{\left(\boldsymbol{V}_i \boldsymbol{u}\right)^2}{2\mathrm{a_s^4}} - \frac{|\boldsymbol{u}|^2}{2\mathrm{a_s^2}}\right] \tag{4.4}$$

where a_s is non-dimensional speed of sound in lattice unit.

PowerFLOW uses a LBM-VLES (Very Large Eddy Simulation) turbulence model for all flow types to resolve structures below the grid filter [13, 55], employing the two equations of the Re-Normalisation Group (RNG) $k-\epsilon$ model. The adopted model is a variant of the classic $k-\epsilon$ formulation [70], which improves its accuracy in complex flows through modifications such as the addition of terms in the epsilon transport equation and reduced standardization in the calculation of the Prandtl number. In lattice methods, such as the one used in PowerFLOW, the effects of sub-grid structures are taken into account through an effective relaxation $\tau_{\text{effective}}$ [13], which involves adding a term linked to turbulent modeling:

$$\tau_{\text{effective}} = \tau_0 + \tau_{\text{turb}} \ , \quad \tau_{\text{turb}} = C_\mu \frac{k^2}{\varepsilon} \frac{1}{T\sqrt{1+\tilde{\eta}^2}}, \quad \widetilde{\eta} = \psi\left(\eta_s, \eta_\Omega, \eta_h \ldots .\right) \tag{4.5}$$

where $C_\mu = 0.08$ and τ_0 is the viscous relaxation time, $\bar{\eta}$, indicative of the time scale of the flow and indicating the uniformity of the turbulence pattern at all flows. Regarding the Reynolds stresses, in LBM solvers these are not added explicitly but arise automatically through the concept of relaxation towards a state of equilibrium (f_{eq}) according to the gas kinetic theory [7].

PowerFLOW divides the fluid domain into refinement zones composed of three-dimensional blocks, or *voxels*, whose size changes between successive voxel refinement (VR) regions by a factor of two. The intersection of solid bodies with the voxels creates surface elements called *surfels*, whose interaction with the fluid particle occurs according to non-slip (bounce-back process) or slip (specular reflection) boundary conditions [55].

Far-field acoustic pressure is obtained using the Ffowcs Williams and Hawkings (FWH) acoustic analogy, implemented in the Farassat 1A formulation [24].

4.2 Experimental Setup

The main study was developed at the Institute of Sound and Vibration Research (ISVR) in Southampton [52], while a new experimental campaign was conducted at TU Delft; therefore, the numerical setup replicates the experimental configuration built at the latter university. The experimental setup (shown in fig. 4.1a) consists of an open-jet wind tunnel placed inside an anechoic chamber, referred to as "A-Tunnel." The walls and ceiling of the chamber are covered with wedges made of absorbent material, as described in detail by Merino-Martínez et al. [44]. The

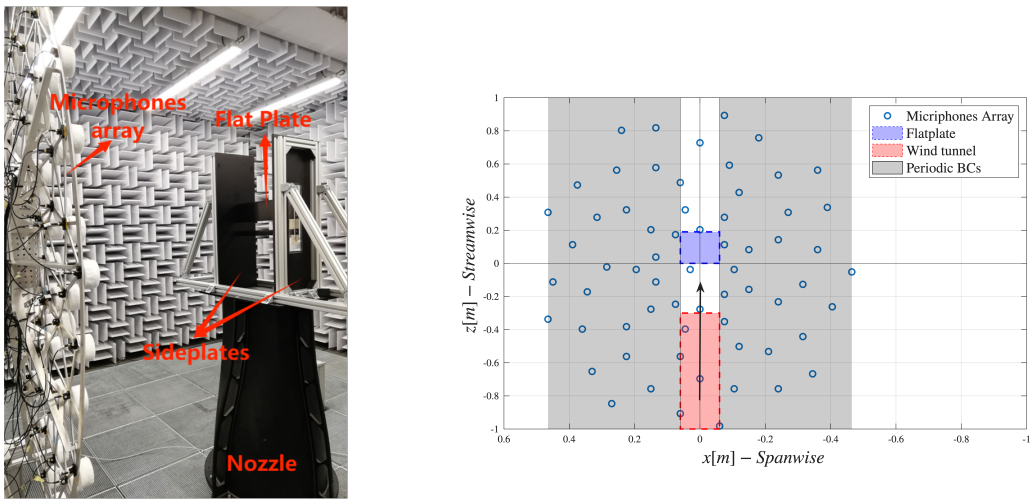

(a) Experimental setup in TU Delft

(b) Microphones position

Figure 4.1: Experimental Setup

nozzle of the open-jet wind tunnel is 1 m long and features a circular inlet section of approximately 0.28 m^2 and a rectangular outlet section of 0.1 m^2. The flat plate is located 0.3 m downstream of the nozzle outlet, where a rectangular turbulence-generating grid is located. The turbulence grid is made of square rods with a cross-section $l = 2 \times 10^{-3}$ m thick with a spacing W of 0.010 m, leading

to a porosity β of 0.69 and a mesh length M of 0.012 m.
The flat plate, made using a 3D printer, has a span of 0.48 m, of which approximately 0.01 m on each side are dedicated to the mounting of the support side plates. The chord is equal to 0.19 m and both the leading edge and trailing edge are chamfered. At a distance of 0.027 m from the leading edge, there is the axis of the hole belonging to the first row of 9. Each hole is imagined at the center of 0.005 m squares, adjacent to each other in both the spanwise and streamwise directions (see Fig. 4.4). The distance between the centers of the first and last holes is 0.040 m; each hole has a diameter of 0.003 m and extends across the entire 0.003 m thickness of the flat plate.
All geometrical information have been summarized in 4.1. It is good to highlight how the turbulence grid is characterized by the porosity β defined in Roach [58] as

Table 4.1: Geometrical characteristics of the experimental setup components.

Wind Tunnel			
Inlet diameter (Φ)	Outlet size		Length (L)
600 mm	250 mm × 400 mm		1000 mm
Flat Plate			
Chord (c_0)	Span (S)	Hole configuration	Thickness (t)
190 mm	480 mm	9 rows, $\Phi_i = 3$ mm	3 mm
Turbulence Grid			
Void length (W)	Rod diameter (d)	Mesh length (M)	Porosity (β) [58]
10 mm	2 mm	12 mm	0.694

$$\beta = (1 - d/M)^2 \tag{4.6}$$

with M mesh Length (M=W+d)and d the size of the rod.
This parameter is very useful in evaluating the Δp pressure drop that is generated through the turbulence grid like we see later.
Acoustic measurements have been obtained by means of the beamforming array shown in Fig. 4.1b). This array features 7 spiral arms of 9 microphones each. The array is parallel to the flat plate at a distance of 1.17 m, centered on the midspan of the flat-plate leading edge. More information about the beamforming array is available in Merino-Martínez et al. [44].
Aerodynamic measurements have been carried out by means of time-resolved PIV with a sampling frequency of 16 480 Hz and a spatial resolution of 0.2576×10^{-3} m. The field of view (FOV) extends from approximately 3×10^{-3} m upstream of the LE to beyond the entire porous zone.

4.3 Numerical Setup

The experimental configuration in figure 4.1a was completely reconstructed in *AutoCAD* and *Fusion 360* obtaining figure 4.2 and was subsequently modified by cutting in the streamwise direction in order to imposing periodic boundary condition, obtaining "2.5D" setup, and reduce computational cost, obtaining only a “slice” of the initial geometry, as shown in Figure fig. 4.3.
In contrast with 2D and 3D simulations, "2.5D" is a misnomer that indicates the simulation of a 3D flow with periodic boundary conditions in one of the 3 dimensions. In our case the "infinity" dimension was spanwise direction. The numerical domain, reproducing the experimental setup, is shown in Fig. 4.3.

It consists of a thin parallelepiped with dimensions, expressed in terms of the chord length c, of $37c$ in the streamwise direction and $24c$ in the vertical direction. A width of 0.12 m was chosen, smaller than the span of the flat plate, to achieve higher spatial resolution near the porous region while keeping the overall computational cost low.
Periodic boundary conditions were applied on the lateral faces of the domain.
This cut, however, was not made arbitrarily, but had to ensure that what comes out of one periodic wall enters the next without realizing the presence of the walls; in other words the periodicity pattern for both the flatplate and the Turbulence grid must be respected. Moreover, the two

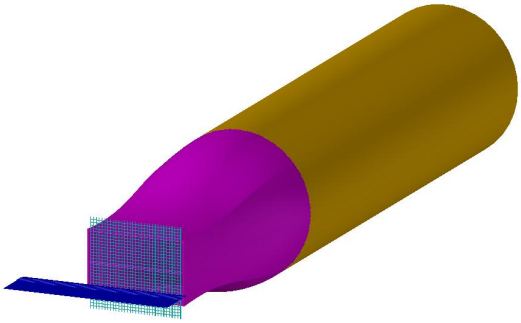

Figure 4.2: Re-building geometry

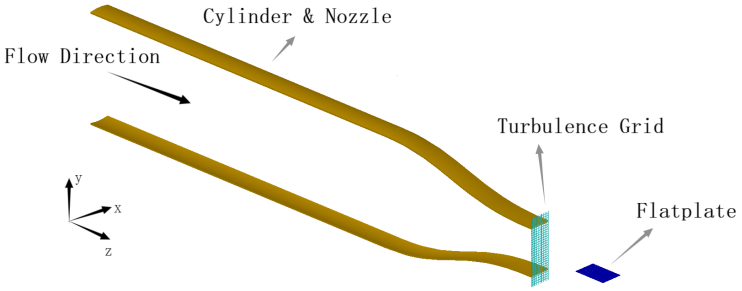

Figure 4.3: Periodic boundary condition and cut of the simulated geometry

periodic walls must not be too close as they would block the development of the homogeneous and isotropic turbulence of the Turbulence grid[1].
In this regard, Blackmore et al. [3] defined a pattern of at least $3M \times 3M$ (where M is the mesh length of the Turbulence Grid), as patterns smaller than the recommended size tend to underestimate the integral length scale and, consequently, the spectral content at low frequencies.
It is possibile to see in fig. 4.2 an additional cylinder before the A-Tunnel nozzle to move the flat plate away from the left wall, avoiding the reflection of acoustic waves.
The reference frame is centered at the midspan of leading edge, with the streamwise, vertical (upwash), and spanwise directions denoted by z, y, and x, respectively. The corresponding velocity components are indicated as w, v, and u.
The refinement regions (see Fig. 4.4) have been arranged to maintain a constant voxel size from the turbulence grid to the flat plate, to avoid numerical effects in the convection of the turbulent structures of the grid. An additional refinement region (indicated as "High resolution" in Fig. 4.4) has been added around the flat plate both for better resolution of the boundary layer, controlled by y^+, and to achieve a resolution of at least $\Delta^+ = 11$ inside the holes according to Jiang et al. [38].It should be noted that y^+ has not been imposed, but is controlled as an output parameter.
As the resolution increases, the number of refinement regions increases in order to preserve 2 voxels in the span direction within the outermost refinement region, and to refine all the other VRs. The voxel size in the refinement zone that extends from the turbulence grid to the flat plate was determined using the studies in Blackmore et al. [3], which show that almost 32 voxels per mesh length M (turbulence grid parameter) are required to correctly develop turbulence downstream of the grid.
Blackmore et al. [3] observed that lower values affect both the turbulent intensities and, to a greater extent, the overestimation of the integral length scale and consequently the low frequencies of the spectra.
The free-stream velocity was set at $20\,\mathrm{m\,s^{-1}}$, and the total pressure, set as a boundary condition at the inlet, was evaluated taking into account the pressure drop induced by grid turbulence. This has been estimated using the empirical expressions of Roach [58], where the Δp across the rectangular

[1] hereinafter referred to as TG

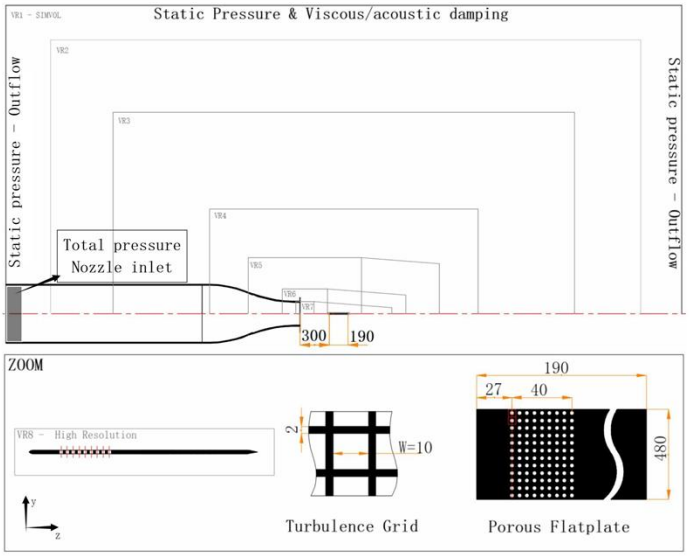

Figure 4.4: Experimental setup in TuDelft

grid, non-dimensionalized with respect to the upstream dynamic pressure q, is expressed as a function of the grid porosity β_{grid} and the coefficients A and B, which are a function of the Reynolds number, Mach number, and grid geometry:

$$\frac{\Delta p}{q_\infty} = A\left(\frac{1}{\beta_{\text{grid}}^2} - 1\right)^B.$$

The static pressure, with the imposition of "Reflection Damping," was set to 101 325 Pa both inside the fluid volume and on the four side surfaces delimiting the simulation volume. Friction inside the separation cylinder and nozzle was neglected, while these effects are present on the turbulence grid and flat plate. The simulation volume has a high-viscosity fluid zone in the upper and lower parts (indicated in Fig. 4.4 as "Viscous/acoustic damping"), which is useful for damping acoustic waves and thus limiting the reflection effect on the domain boundaries. The distance of this damping zone from the flat plate was chosen to be sufficiently large to prevent this viscosity from altering the flow through and out of the nozzle.
The simulation time was determined in terms of flow passes (FP), defined as the time it takes for the particle to travel a distance equal to the chord at the free-stream velocity. The convergence of the lift coefficient was chosen as the control variable to define the simulation time. In order to reduce the computational load, the "*seeding*" technique was used, which consists of using lower resolution results as input in a higher resolution simulation, reducing transition time. The finest resolution simulation, began with 15 FPs followed by 47 FPs during which the data have been saved and sampled at 201 kHz.
All simulation has a physical simulation time of 0.589 s.

The main information about all the simulations carried out is reported in the table 4.2.

Table 4.2: Refinement

Refinement level	**Nº voxel**	**CPU time [h]**	**Voxels/hole**	**Smallest voxel** [m]
Medium [Snellius (NL)]	$\sim 0.2 \times 10^9$	1.37×10^4	12.8	2.34×10^{-4}
Fine [Legion (IT)]	$\sim 1.5 \times 10^9$	2.57×10^4	25.5	1.17×10^{-4}

4.4 Post-processing

For the sake of clarity in presenting the results that follow, this section outlines the mathematical tools employed, highlighting only the properties most relevant to understanding the phenomena under study. The frequency–wavenumber spectrum, used to visualize the spectral components of hydrodynamics and near-field acoustics, is evaluated through a multidimensional space–time Fourier transform of the pressure jump fluctuations between the two faces of the flat plate as:

$$\Delta p'(f,k) = \int_{-\infty}^{\infty}\int_{-\infty}^{\infty} \Delta p'(t,x) e^{-j(2\pi f t - k\cdot x)}\, dt\, dx \tag{4.7}$$

where $\Delta p'$ is evaluated as $\Delta p - \bar{\Delta p}$, k is the wavenumber, f is the frequency, and t is the time. According to Shubham et al. [62], after performing the Fourier transform using Eq. 4.7, it is possible to separate the acoustic and hydrodynamic contributions by applying a top-hat filter in the Fourier space $Y(f,k)$, as shown in Eq. 4.8. This is followed by a return to the time domain through a double inverse Fourier transform, as indicated in Eq. 4.10:

$$\Delta p\prime_Y(f,k) = \Delta p\prime(f,k) Y(f,k) \tag{4.8}$$

$$Y(f,k) = \begin{cases} 1 & f_{\text{lowerband}} \leq f \leq f_{\text{upperband}} \\ 0 & f \geq f_{\text{upperband}} \\ 0 & f \leq f_{\text{lowerband}} \end{cases} \tag{4.9}$$

$$\Delta p\prime_Y(t,x) = \mathcal{F}^{-1}\left[\Delta p\prime_Y(f,k)\right]^{2} \tag{4.10}$$

where $Y(f,k)$ stands for the filtering coefficient, taking values of either 0 or 1, and $\mathcal{F}^{-1}$ stands for the Fourier inverse transform. The lower and upper bands of the filtering coefficient delineate the threshold range, which is determined by the phase velocities of the convective velocity U_c and the speed of sound a_0, as illustrated in the section dedicated to convection velocity.
This method can be repeated three times to separate the contribution of the hydrodynamic pressure jump from the acoustic contributions related to the retrograde and progressive waves. In other words, it can be written as:

$$\Delta p_Y(t,x) = \Delta p_{hy} + \Delta p^{+}_{ac} + \Delta p^{-}_{ac} \tag{4.11}$$

where $_{hy}$ represents the hydrodynamic component and $_{ac}$ represents the acoustic components. The hydrodynamic waves propagate at a velocity close to the convective velocity U_c, while the upstream (p^{-}_{ac}) and downstream (p^{+}_{ac}) traveling acoustic waves move at $U_c - a$ and $U_c + a$, respectively, as can also be observed from the frequency–wavenumber spectrum.

A pivotal analysis of this thesis, as will be described in detail later, is the study of the phase shift between the acoustic sources. This shift is evaluated as the phase $\theta_{\Delta p}$ of the Cross-Power Spectral Density (CPSD), defined as follows in Eq. 4.12:

$$G_{\Delta p \Delta p}(z,\Delta z,f) = \int_{-\infty}^{\infty} \langle \Delta p(z,t) \Delta p(z+\Delta z, t+\tau)\rangle \mathrm{e}^{-\mathrm{i}f\tau}\, \mathrm{d}\tau \tag{4.12}$$

In Equation 4.12, $i = \sqrt{-1}$ is the imaginary unit, and the operator $\langle\cdot\rangle$ denotes the ensemble average over the streamwise separation distance, z. In the spectral calculations, a Hanning window function is applied before the pressure signals are Fourier-transformed.

The analysis of the phase shifts between acoustic sources will be conducted by taking into account the streamwise coherence length, evaluated through Equation (4.13):

$$l_z(\omega) = \int_0^{\infty} \gamma(\xi,0,\omega) d\xi \tag{4.13}$$

where $\gamma(\xi,0,\omega)$ represents the coherence function defined, in its most complete form, as in 4.14:

$$\gamma^2(\xi,\eta,\omega) = \frac{|G_{\Delta p \Delta p}(\xi,0,\omega)|^2}{\phi(\omega)^2} \tag{4.14}$$

where $\phi(\omega)$ is the single-point spectrum at the reference point and $|G_{\Delta p \Delta p}(\xi,0,\omega)|$ is the cross-spectral density, with $\boldsymbol{\xi} = (\xi,\eta)$, where ξ and η represent the spatial separations in the streamwise and spanwise directions, respectively.

[2] From this point forward, the prime ' indicating fluctuations will be omitted for simplicity

Chapter 5

Validation of the numerical simulation

"Addò c'è gusto nun ce sta perdenza": Dove c'è gusto non c'è perdita (i sacrifici per passione valgono la pena)"

— DETTO NAPOLETANO

In this chapter, the agreement between the numerical results and the experimental data is verified by comparing several parameters. Additionally, a grid convergence study is performed.

5.1 Aerodynamic validation

The comparison of the aerodynamic data, namely the *integral length scale, turbulence intensity and streamwise-velocity spectrum* is carried out considering the flow characteristics at $z/c = -0.0135$ and $y/c = 0.0863$, i.e., at the red point in 5.1. The measurement point was placed as far as

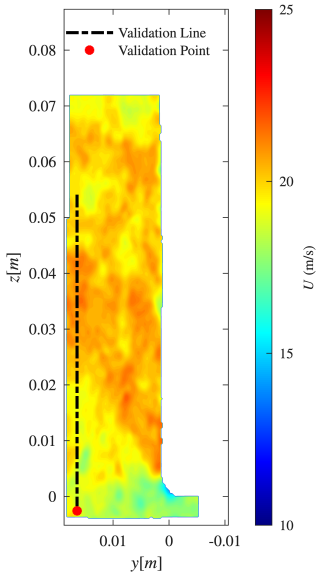

Figure 5.1: PIV and some indications about matching activity

possible from the flat plate to avoid distortions induced by both numerical factors (boundary-layer modeling, body penetration into the voxels) and experimental limitations (PIV resolution).
The integral length scale in the streamwise direction L^z_{ww} has been evaluated by means of the expression 5.1:

$$L_{ww}^{z}(\boldsymbol{z},l)=\int_{0}^{\infty}R_{ww}^{z}(\boldsymbol{m})\mathrm{d}l=\int_{0}^{\infty}\frac{\overline{u_z\left(\boldsymbol{z}+\boldsymbol{l}\boldsymbol{e}_m\right)u_z(\boldsymbol{z})}}{u_z(\boldsymbol{z})u_z(\boldsymbol{z})}\mathrm{d}l \tag{5.1}$$

where $R_{ww}^{z}(\boldsymbol{m})$ is the correlation coefficient calculated considering a reference location z, u_z is the turbulent velocity fluctuations components in the z directions e_m is the unitary vector in the mth direction, $\mathbf{le}_m$ is the separation length from the reference location.
As usually indicated in Hinze [37], these Eulerian correlations are evaluated at a fixed instant in time if, as in this case, the time dependence is omitted; in other words, one can imagine that all the quantities in Equation (5.1) are time-dependent.
The average used in the convolution product always represents an ensemble average. Given the impracticality of performing such an operation, the ergodicity theorem is invoked so that it can be assimilated to a temporal or spatial average [48].
A temporal or spatial average will be chosen, respectively, if the flow is statistically stationary or homogeneous at least in the direction along which the convolution develops. In the present case, the well-known statistical homogeneity in the streamwise direction leads to the choice of a spatial average taken along the black line shown in Figure 5.1.
The turbulent intensity associated with the streamwise fluctuation has been evaluated as $\mathrm{T}_w = \sqrt{\overline{w'^2}}/\overline{W}_\infty$. This flow quantity, together with L_{ww}, has been used to estimate the von Karman spectrum of the streamwise velocity component, whose expression is reported hereafter

$$\Theta_{ww}\left(k_z\right)=\frac{1}{\sqrt{\pi}}\frac{\Gamma(5/6)}{\Gamma(1/3)}\frac{\overline{w^2}}{k_\mathrm{e}}\frac{1}{\left[1+\left(k_z/k_\mathrm{e}\right)^2\right]^{5/6}}. \tag{5.2}$$

Γ is the Gamma function, k_z is the wavenumber in the streamwise direction, and k_e is defined as the wavenumber scale of the largest eddies according to the expression:

$$k_\mathrm{e}=\frac{\sqrt{\pi}}{\mathrm{L}_{ww}}\frac{\Gamma(5/6)}{\Gamma(1/3)} \tag{5.3}$$

The comparison between the time-averaged free-stream velocity, the integral length scale and the turbulence intensity obtained numerically and experimentally is reported in Tab. 5.1, showing good agreement.

Table 5.1: Experimental-numerical comparison of flow parameters.

Activity	$\bar{W}_\infty$ **(m/s)**	L_{ww} **(m)**	T_w **(%)**
Experimental PIV	19.18	0.0057	3.3
Numerical LBM-VLES *(Medium)*	19.10	0.0062	3.9
Numerical LBM-VLES *(Fine)*	19.80	0.0063	3.0

Figure 5.2 reports the one-dimensional wavenumber spectrum of the streamwise-velocity component fluctuations calculated numerically, experimentally and analytically by means of the von Karman expression near the leading edge, as previously explained.

The similar trends of the two curves obtained from the numerical simulation demonstrate good grid convergence, confirming what was previously reported in Table 5.1
The slight discrepancies at low and high frequencies can be attributed respectively to a different simulation time length and to the presence of a much narrower grid filter in the case of the *fine* resolution.
Analyzing the two issues separately, it is important to remember that an insufficient simulation time would prevent the development of long-wavelength harmonics, while the application of a very wide filter, as in the case of the *medium* resolution, would cause relatively large structures to be modeled, with a consequent reduction in intensity.
Comparing the spectrum obtained by extracting data from the PIV processing with the spectra from the numerical processing, an overestimation and underestimation at low and high frequencies, respectively, can be observed. This behavior is fully confirmed by Xu and Chen [72], who attributed—and subsequently corrected—the problem to PIV windowing, which acts as a filter.
Finally, the dashed golden curve represents the von Kármán (VK) spectrum (Eq. 5.2), evaluated

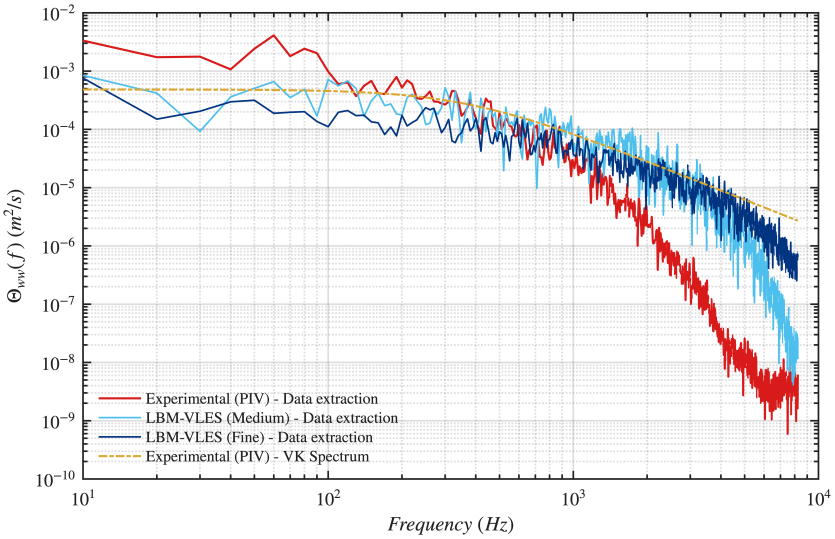

Figure 5.2: Spectral comparison

using parameters derived from the experimental activity. It shows better agreement with the numerical spectrum than with the experimental one. Since the VK spectrum is a model that uses integral and averaged quantities, such as L_{ww} and $\bar{w}'$ respectively, as characteristic flow parameters, it is significantly less sensitive to filtering effects. For completeness, Fig. 5.3 also shows the behavior of the correlation curves evaluated at the red point and along the black curve in Fig. 5.1. Similarly to what was observed in the previously described spectra, the correlation function evaluated using experimental data also tends to intersect the numerical ones, showing an underestimation of coherence over longer distances. This can be attributed to a higher diffusion of high-frequency structures and scales.

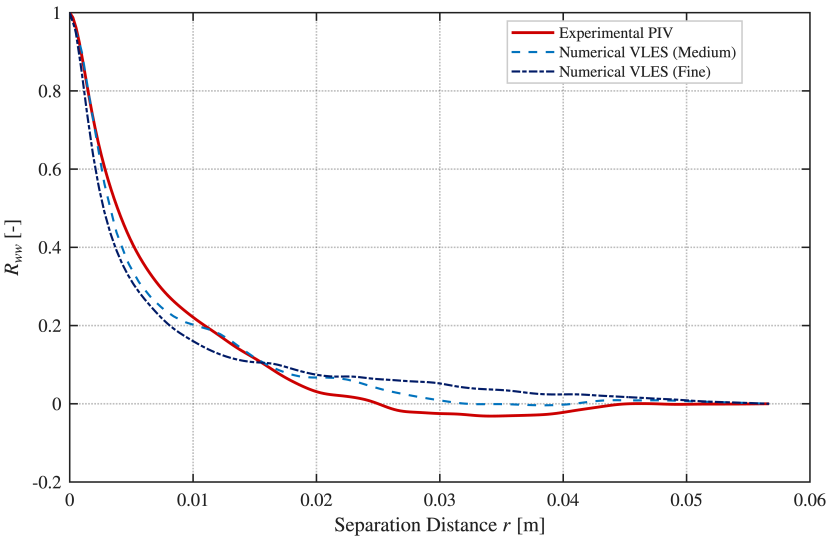

Figure 5.3: Correlation coefficient

5.2 Acoustic Validation

Acoustic validation was performed considering the sound pressure level (SPL) of the noise in the far field at the central point ($x = 0$), near the trailing edge (0.209 m) at a height y, constant for all microphones, of 1.171 m.
Because periodic boundary conditions were applied, only a subset of the full plate span was modeled, it was necessary to introduce a correction to account for the resulting changes in scattering,

in a way similar to the approach used in Jiang et al. [39].
Accordingly, the SPL obtained using the FWH analogy ($\mathrm{SPL_{FWH}}$) was corrected by an additional term $\mathrm{SPL_{corr}}$, leading to the following expression for the overall numerical SPL:

$$\mathrm{SPL_{num}} = \mathrm{SPL_{FWH}} + \mathrm{SPL_{corr}}. \tag{5.4}$$

The correction term $\mathrm{SPL_{corr}}$ is evaluated as:

$$\mathrm{SPL_{corr}} = \begin{cases} 10\log(N) & (l_x/L_{num} \leq 1/\sqrt{\pi}) \\ 10\log(\sqrt{\pi}N) + 10\log\left(l_x/L_s\right) & (1/\sqrt{\pi} < l_x/L_{num} < N/\sqrt{\pi}) \\ 20\log(N) & (l_x/L_{num} \geq N/\sqrt{\pi}) \end{cases}, \tag{5.5}$$

where $N = L_{\mathrm{exp}}/L_{\mathrm{num}}$ denotes the ratio between the experimental airfoil span L_{exp} and the numerical airfoil span L_{num}. The value obtained for the spanwise correlation length l_x, estimated from the spanwise coherence function of the surface pressure over the porous region, led to the calculation of $\mathrm{SPL_{corr}}$ through the second expression of Eq. 5.5.

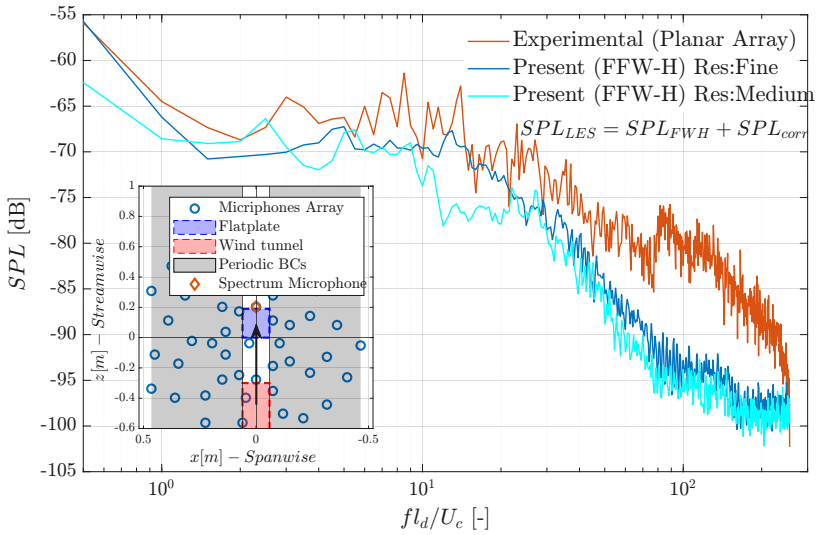

Figure 5.4: Acoustic Matching

The resulting SPL is presented in Fig. 5.4, where it is compared with the experimental measurements. Good agreement is observed between the numerical and experimental spectra trend, despite the aerodynamic discrepancies discussed above and the applied SPL correction. Similar to the velocity spectra, poorer agreement is observed in the high-frequency range, which is attributed to the numerical filtering associated with the grid resolution. It is important to point out a slight reduction in the numerical SPL compared to the experimental one, which may be traced back to the side plates. These were placed in the experimental setup to support the flat plate and were not considered in the numerical setup. The presence of the side plates is not accounted for by the previously mentioned correction; indeed, as stated by Seo and Moon [61], that correction only accounts for the difference in spanwise extent between the numerical and experimental domains. Additionally, it must be considered that the experimental uncertainty range was not declared by the author. Nevertheless, the difference between the numerical and experimental acoustic signatures is very small (approximately 1.5 dB), confirming a good acoustic match.

5.3 Alteration of turbulence induced by periodic BC

This section aims to quantify and further investigate the distortion of homogeneous and isotropic turbulence resulting from the presence of periodic boundary conditions, validating a study that analytically demonstrated the incompatibility between these two quantities.

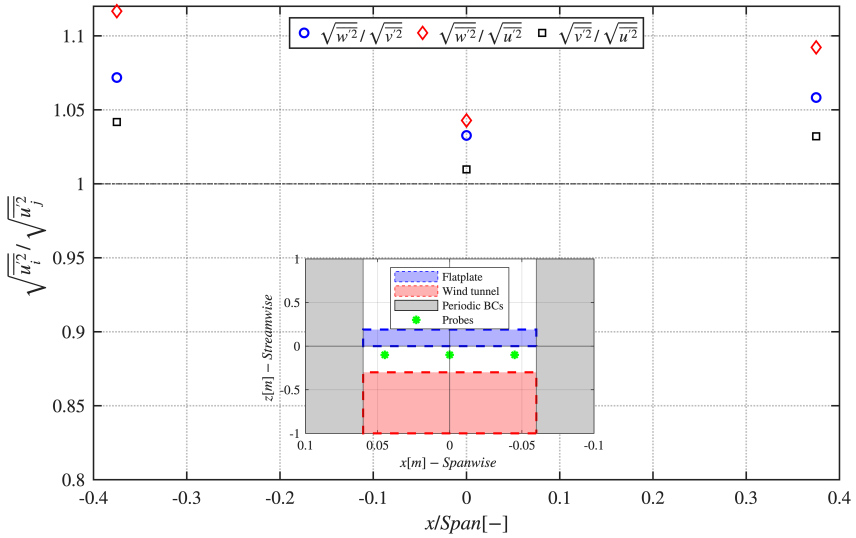

Figure 5.5: RMS of Fluctuation velocity

5.3.1 Distortion quantification

The effect of the periodic boundary conditions can be evaluated by considering the spanwise distribution of the root-mean-square (RMS) of the velocity fluctuation components in the three coordinate directions. Specifically, velocity fluctuations are sampled near the boundaries, at $x/L_{span} = \pm 0.37$, and at the center of the jet, $x/L_{span} = 0$.

The choice of the z/c coordinate was dictated by the need to maintain a sufficient distance from the turbulence grid to ensure the full development of homogeneous isotropic turbulence. However, this positioning resulted in a proximity to the flat plate, which likely influenced the measurements, as discussed further below. It should be noted that as the freestream velocity decreases, the distance required for the full development of turbulence increases.

The plot in Figure 5.5 shows that at the center of the wind tunnel, the RMS ratios are close to unity, in agreement with the hypothesis of homogeneous isotropic turbulence. The proximity to the flat plate introduces distortions that are inseparable from those induced by the periodic boundary conditions (BCs), preventing a perfectly unitary ratio.

Conversely, as the lateral periodic walls are approached, the ratios tend to shift, increasing by approximately 10%. This trend is consistent with the findings reported in Qin et al. [57]. This observation highlights an intensification of fluctuations in all directions; however, further investigation is required to fully characterize the underlying cause of this phenomenon.

5.3.2 Form of Distortion - Lumley's Triangle

The analysis of distortion proceeded by evaluating the type and shape of anisotropy induced by the periodicity conditions. To ensure a comprehensive understanding, a description of the mathematical tools employed is provided below.
The concept of isotropy mentioned above is characterized by various theoretical formulations that essentially express the same principle. In Simonsen and Krogstad [63], it is defined by the Reynolds stress tensor R_{ij} which is spherical, meaning that it has no off-diagonal terms, while in Nosrati et al. [49], it is represented by the rotational invariance of the normal components of the Reynolds stress. This implies that in order to study the nature and the degrees of anisotropy of a symmetric second-order tensor (matrix), it is necessary to investigate the off-diagonal terms of the Reynolds stress tensor. The most effective method for this is to adopt the well-known "Anisotropy Invariant Map (AIM)" or Lumley triangle, as described in Andersson and Karlsson [2].
The AIM represents the space within which all possible states of turbulence, including the isotropic state, are constrained to lie, expressed in terms of the principal invariants.
Some key information regarding the Lumley triangle is provided below.
Any second-order tensor τ_{ij} can be rewritten as the sum of its isotropic component τ_{ij}^{o} and its

deviatoric component τ'_{ij} [63]:

$$\tau_{ij} = \tau^{\circ}_{ij} + \tau'_{ij}$$

where the isotropic part is defined as:

$$\tau^{\circ} = \frac{1}{3}\tau_{kk}\delta_{ij}$$

while the deviatoric part is:

$$\tau'_{ij} = \tau_{ij} - \frac{1}{3}\tau_{kk}\delta_{ij}$$

By non-dimensionalizing the deviatoric part, we obtain the "Reynolds stress anisotropy tensor," which forms the basis of the AIM:

$$b_{ij} = \frac{\tau'_{ij}}{\tau_{kk}} = \frac{\tau_{ij}}{\tau_{kk}} - \frac{1}{3}\delta_{ij}$$

characterized by having orthonormal eigenvectors along the principal directions and real eigenvalues λ_i [2].
By using the Cayley-Hamilton theorem, the characteristic equation for any second-order symmetric tensor may be written as

$$\sigma^3 - I_1\sigma^2 + I_2\sigma - I_3 = 0$$

where the I 's are the first, second, and third invariants of the tensor and σ is the principal stress.
It is important to emphasize the meaning of the numbers under the eigenvalue symbol: $1, 2, 3$ refer to the streamwise, vertical, and spanwise directions, respectively.
The invariants are related to tensor terms b_{ij} and to the eigenvalue of *anisotropy* tensor λ_i as:

$$\mathrm{II} = -\frac{b_{\mathrm{ij}}b_{\mathrm{ij}}}{2} = -\left(\lambda_1^2 + \lambda_1\lambda_2 + \lambda_2^2\right)$$
$$\mathrm{III} = \frac{b_{\mathrm{ij}}b_{\mathrm{jk}}b_{\mathrm{ki}}}{3} = -\lambda_1\lambda_2\left(\lambda_1 + \lambda_2\right)$$

The AIM is visualized as a triangle (as in Figure 5.6) on a $(III, \text{-}II)$ plane, with $I2$ denoting the level of anisotropy and III representing the type of anisotropy.
The three segments presented in Figure 5.6 can be derived as:

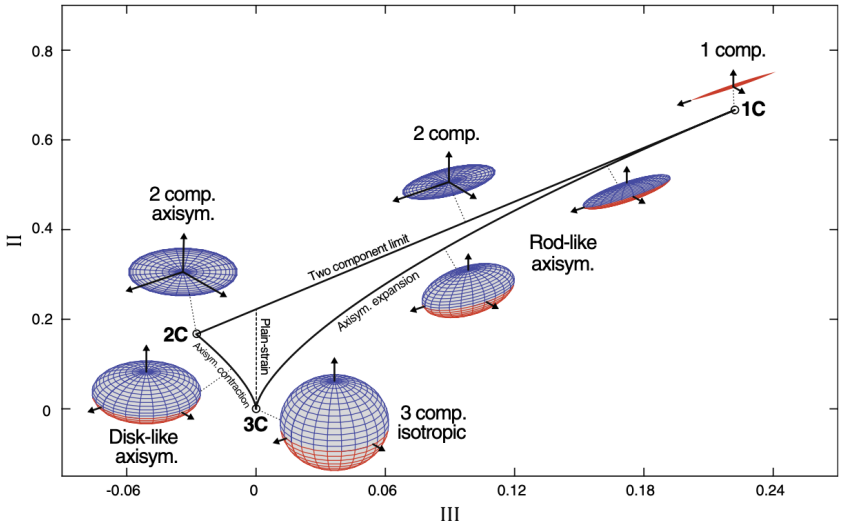

Figure 5.6: Example of Lumley triangle [2]

$$\text{III} = -2\left(-\frac{\text{II}}{3}\right)^{3/2} \qquad \text{left boundary (axisymmetric contraction)}$$

$$\text{III} = 2\left(-\frac{\text{II}}{3}\right)^{3/2} \qquad \text{right boundary (axisymmetric expansion)}$$

$$\text{III} = -\frac{9\text{II}+1}{27} \qquad \text{upper bound (two-component turbulence)}$$

Developing the calculation for the case under examination yields the result shown in Figure 5.7.

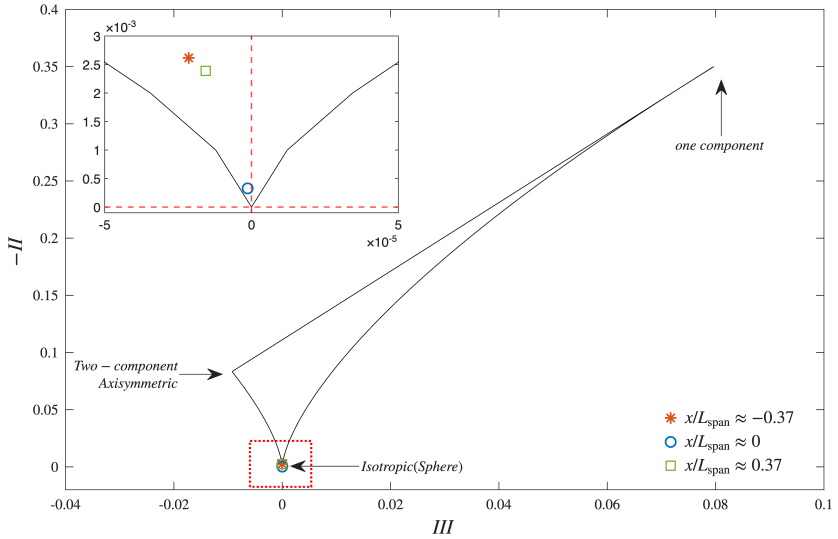

Figure 5.7: Lumley triangle

It is evident that the sampled velocity fluctuations at the center of the wind tunnel can be traced back to a spherical, and therefore isotropic, tensorial state, placing the blue circle at the bottom exactly where the invariants of the anisotropic tensor are zero.
Sampling at the other two points, on the other hand, leads to a clear shift to the left, that is, to negative values of the $3rd$ invariant, which should be recalled is indicative of the type of anisotropy. This shift indicates that the stress state tends toward a "disk-like," also known as "pancake-like," configuration, with 2 main stress axes.
Periodic conditions tend to produce a stretching of the fluid element, altering its isotropic state. To confirm this, it was decided to evaluate the stresses directions by studying the rotation of the eigenspace, as described in the next paragraph.

5.3.3 Stress Direction and vortex stretching

As is well known, the eigenvectors of the anisotropy stress tensor represent the directions along which the stress, identified by the eigenvalues, acts.

These eigenvectors generate the eigenspace, which will naturally be rotated with respect to the coordinate axes. Therefore, it is first necessary to identify the eigenvectors associated with the eigenvalues of the largest magnitude (consistent with the previous analysis), bearing in mind that the display triad is defined as $[z\ y\ x]^T$.

From the results presented in Table 5.2, it is evident that two eigenvalues are significantly larger than the third at both sampling locations. This is in agreement with the "pancake-like" stress state analyzed in the previous section.
Correspondingly, the components of the individual eigenvectors associated with these dominant eigenvalues are analyzed to determine their primary directions of action.
It should be noted that each eigenvector (represented by a column in the matrix) is composed of three components, which represent the projection of the vector onto the coordinate axes defined in Chapter 4.
It is clearly observed that the y-component is nearly zero, indicating that the resulting vector for each eigenvalue lies within the $[z; x]$ plane of the flat plate. Furthermore, the rotation of these

Eigenvector $(x/L_{span} = -0.37)$	**Eigenvector** $(x/L_{span} = +0.37)$
$\begin{pmatrix} \mathbf{-0.3620} & 0.1041 & \mathbf{-0.9264} \\ 0.0020 & 0.9938 & 0.1109 \\ \mathbf{-0.9322} & -0.0383 & \mathbf{0.3600} \end{pmatrix}$	$\begin{pmatrix} \mathbf{-0.4392} & 0.0722 & \mathbf{0.8955} \\ 0.0292 & 0.9974 & -0.0660 \\ \mathbf{0.8979} & 0.0029 & \mathbf{0.4401} \end{pmatrix}$
Eigenvalue $(x/L_{span} = -0.37)$	**Eigenvalue** $(x/L_{span} = +0.37)$
$\begin{pmatrix} \mathbf{-0.0464} & -0.0084 & \mathbf{0.0548} \end{pmatrix}$	$\begin{pmatrix} \mathbf{-0.0452} & -0.0066 & \mathbf{0.0519} \end{pmatrix}$

Table 5.2: Anisotropic stress tensor eigenvectors and eigenvalues at $x/L_{span} = \pm 0.37$

vectors within the plane is minimal, as there is consistently one component (z or x) that tends toward unity, aligning the unit vector closely with that specific coordinate axis.
This implies that the rotation of the eigenspace relative to the coordinate axes is very small; this confirms that the primary stretching occurs in the x and z directions—specifically, the spanwise direction, driven by the periodicity conditions, and the streamwise direction, caused by the mean flow development. The effect of this phenomenon can be observed in the average vorticity. Figure

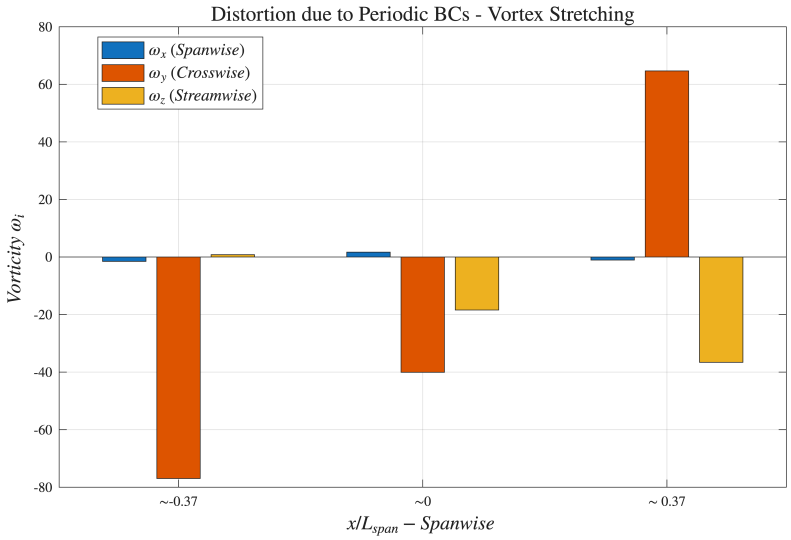

Figure 5.8: Vortex Stretching-Tilting

5.8 shows the value of the average vorticity in the three directions, which highlights the presence of strong vorticity in the y-direction at the two lateral points.

This phenomenon is known as Tilting (or twisting), which is a three-dimensionalization of the vorticity resulting from the deformation of the fluid element induced by velocity gradients $\nabla \boldsymbol{u}$. Indeed, it should be recalled that vorticity acts through mechanisms known as "Vortex Stretching" and "Vortex Tilting/Twisting" generated by the term on the right-hand side of the vorticity equation 5.6:

$$\frac{\mathrm{D}\boldsymbol{\omega}}{\mathrm{D}t} = \boldsymbol{\omega} \cdot \nabla \boldsymbol{u} \tag{5.6}$$

"Vortex stretching", according to Tritton [68], is associated with the terms $\frac{\partial u_i}{\partial x_i}$, which cause an elongation/shortening of the fluid element along an axis, inducing an increase in vorticity along that same axis. Tilting, on the other hand, is associated with the cross-terms of the velocity gradient, namely $\frac{\partial u_i}{\partial x_j}$.
In the present case, it appears that the primary behavior is, as previously mentioned, tilting, since stresses in the spanwise and streamwise directions activate strong vorticity in the crosswise direction.

Chapter 6

Results

"San Nicola proteggici da l rizz vacand "
— Preghiera barese

As clearly highlighted in the literature review, one of the most significant fluid-dynamic patterns in the flow over porous surfaces are Kelvin-Helmholtz (KH) waves—structures characterized by highly non-linear dynamics. These non-linear dynamics have proven to be a fundamental factor in noise generation, as emphasized in the literature study. Therefore, this chapter begins by demonstrating, both mathematically and graphically, the presence of KH instabilities, characterizing the mean velocity profiles within the pores. These profiles lead to a more in-depth analysis of the convection velocity, which is crucial for defining the Strouhal number (St). The analysis will proceed by discussing the near-field acoustic cone and its alteration induced by a potential cut-off mechanism. The study concludes with an investigation of the phase shifts of the acoustic sources, following a decomposition of the near-field acoustics from the hydrodynamics.

6.1 Flow Characterization

A visual analysis of the main flow features will be reported in order to provide a better understanding of the subsequent results.
The trend of the mean velocity and the root mean square of the velocity fluctuations were considered to quantify the motion inside the holes. As shown in the image in Figure 6.1, a down-upwash phenomenon emerges, which gradually intensifies as it proceeds towards the end of the porous section. What is visible in the images is not indicative of the specific type of motion (upwash or downwash), since these are time-averaged quantities; rather, it reflects the presence of motions with varying intensities that alter the boundary layer by transporting momentum towards or away from it.
The presence of fluid penetration is not only a prerogative of turbulence (represented by the RMS of the fluctuations), but also of the mean flow. A similar behavior was observed in the experimental work by Feng and Ye [25]; who studied a flat plate with non-through (blind holes) anisotropic porosity, in contrast to the flat plate analyzed in this thesis, where through-holes are placed.
As analyzed in the studies in the previous section, these phenomena, by altering the boundary layer, modify the coherent structures and can induce forms of instability. For this reason, an attempt was made to investigate the presence of possible instability mechanisms.

Figure 6.2 depicts the value of the second derivative with respect to y of the mean velocity U_z ($d^2\bar{U}_z/dy$) and the presence of a zero point between the holes and the overlying boundary layer. In accordance with Rayleigh's criterion as presented in Drazin and Reid [17] and Criminale et al. [15], an inflection point in the velocity profile is a necessary (but not sufficient) condition for the instability of an inviscid flow, at least for the case of unidirectional laminar flow in a meanly homogeneous zone. Therefore, these inflections may lead to Kelvin-Helmholtz instabilities, similar to other works such as Breugem et al. [4]. In figure 6.3, the mean streamwise velocity profiles sampled inside the holes starting from 2.5 mm below the surface of the flat plate are shown. The change in concavity is visible (from concave downward when looking inside the hole, and the

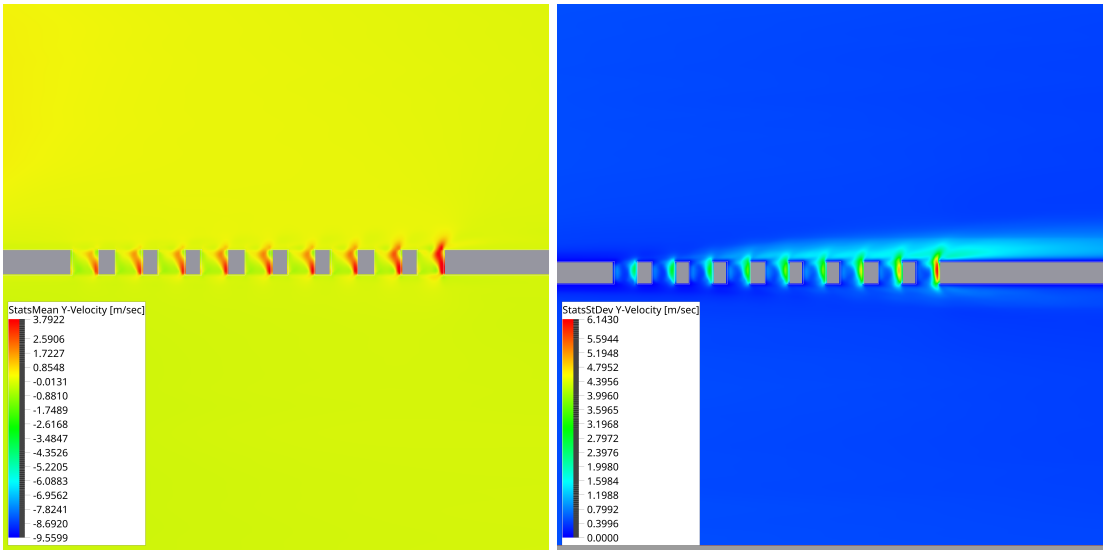

(a) Mean value of vertical velocity (b) RMS of vertical fluctuation

Figure 6.1: Vertical inflow

opposite when looking toward the upper part of the flat plate). A mean velocity reduction is visible too. A more in-depth analysis of the variation in mean velocity is carried out below with different mathematical tools as this velocity reduction plays an important role in this analysis.

The alteration of the boundary layer caused by upwash and downwash phenomena can lead to the triggering of KH instabilities; therefore, to gain a deeper insight into this process, it was decided to investigate the mechanism through a series of snapshots of the instantaneous spanwise vorticity, evaluated at the midspan near a row of holes.

A key role in the boundary layer alteration is played by the penetration of negative vorticity (blue in the figure) into the boundary layer developed on the upper face of the plate. In fact, as will be described more thoroughly later, the phenomenon of vorticity penetration through the pores alternates periodically from the lower face to the upper face and vice versa, like a shedding.

As clearly visible in Figure 6.4a, the vorticity penetration becomes progressively more intense towards the holes located at the end of the porous zone. This is due to a less energetic and slower flow over the plate, resulting in a reduced momentum capable of opposing the flow penetrations.

A recurring behavior underlying the generation of instabilities appears to be the interaction of the two vorticities (red and blue) in a suction mechanism, as shown in Figure 6.4a. As schematically depicted in the zoom in Figure 6.4a, the two vortex structures within the hole might be concurrent at the point of contact to such an extent that they draw fluid from the upper part of the flat plate into the hole. This manifests as a lowering of the fluid line, as shown within the white squares. This behavior would accelerate the fluid to the left—opposite to the freestream direction—thereby confirming and justifying the negative velocity near the edge of the hole visible in Fig. 6.3, and consequently the change in the inflection point.

By drawing fluid into the holes, the conditions are created for a structure such as the one indicated by the black arrow in Figure 6.4a,where a high-velocity fluid tends to rise above the underlying fluid.

The described mechanism, with drawing of fluid, also appears after a few moments, as seen in the orange box in Figure 6.4b near the first hole. This generates an unstable structure that grows, moves by convection, and becomes clearly defined in Figure 6.4c and Figure 6.4d (orange box), where an intense vortex core (red) is visible, surrounded by less intense vorticity and filaments known as *braids* [34].

Continuing its path toward the exit of the porous zone, the tracked structure tends to be stretched and elongated (Figure 6.4f), increasing in size until the growth collapses. This is observed for the structure positioned further ahead (labeled "structure tracking 2") when transitioning from the instant in Figure 6.4f to that in Figure 6.4g. It is worth noting that fluid dynamics is a phenomenon that tends toward a state of stability; as such, every growth is transient and cannot increase indefinitely.

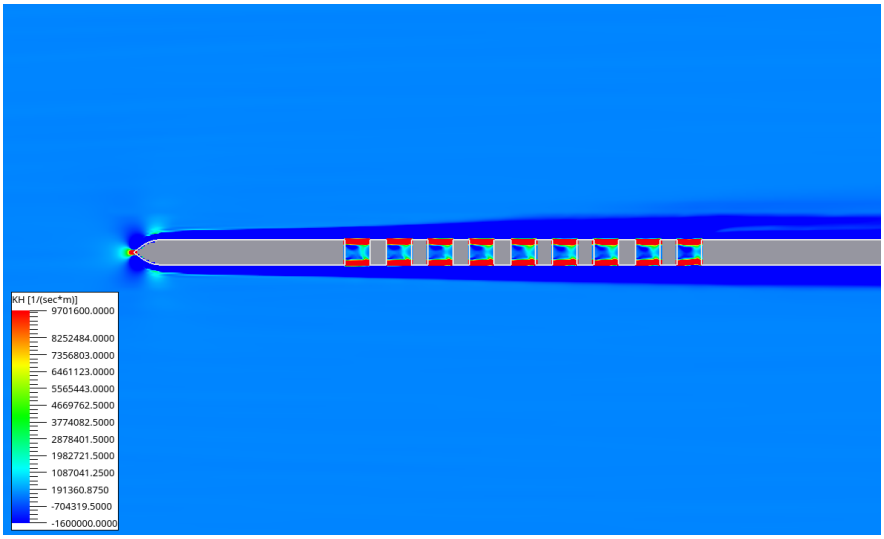

Figure 6.2: Inflection point $d^2U_z/d^2y = 0$

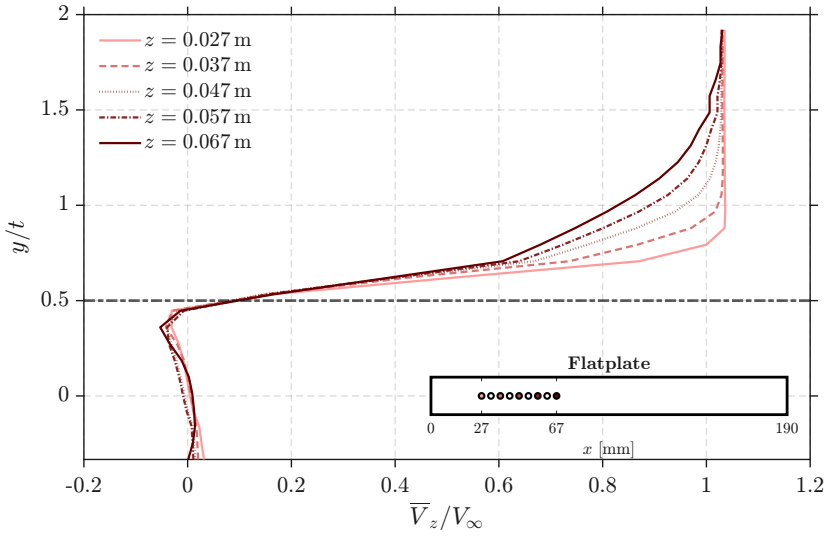

Figure 6.3: Streamwise velocity profile through the holes

Naturally, the various structures influence one another, leading to more or less intense growth depending on their interaction. Indeed, after several timesteps, the transient growths are such that the vorticity becomes completely fragmented, presenting both positive and negative vorticity structures on the upper side as in Figure 6.5, where an alternate shedding motion is present. This fragmentation has been attributed to the $e^{i\pi}$ phase shift, introduced by Palleja-Cabre et al. [52] in his analytical model.

6.2 Study on the alteration of convection velocity

The entire experimental study carried out by Palleja-Cabre et al. [52] is based on the identification of acoustic reduction peaks near integer Strouhal numbers, with Strouhal defined as fl_d/U_c, where l_d represents the distance between the leading edge and the end of the porous zone and U_c is the convection velocity (i.e., the transport/convection speed of turbulence), assumed in the experimental study to be $0.7 \cdot U_\infty$.
Following the methodology established by Kang and Lee [40] and Shubham et al. [62], the frequency-wavenumber spectrum of the pressure jump fluctuations between the two faces of the flat plate was evaluated. This was achieved via a multidimensional Fourier transform of the space–time flow field

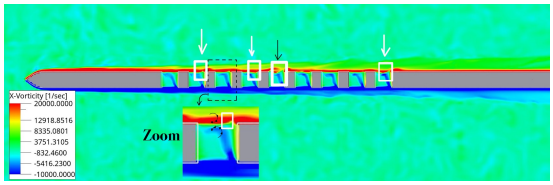

(a) $t_0 = 0.189259$s

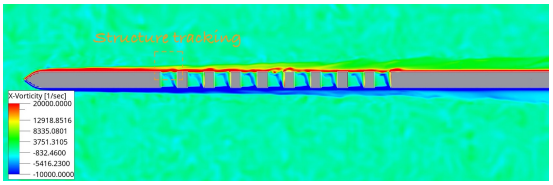

(b) $\Delta t_1 = 0.103$ms

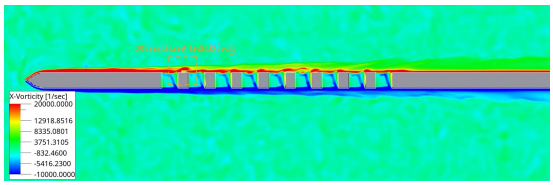

(c) $\Delta t_3 = 0.4ms$

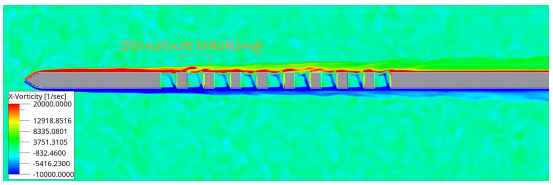

(d) $\Delta t_4 = 0.568ms$

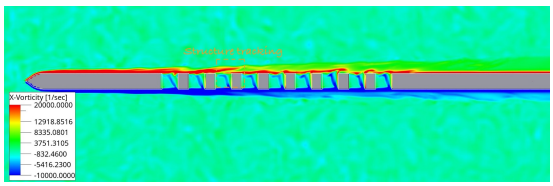

(e) $\Delta t_5 = 1.29ms$

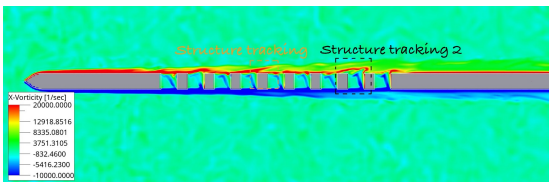

(f) $\Delta t_6 = 2.06ms$

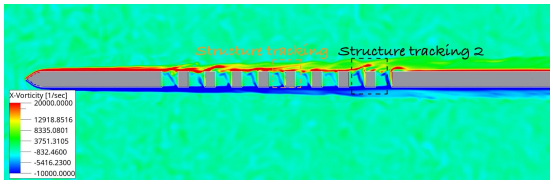

(g) $\Delta t_6 = 2.42ms$

Figure 6.4: Temporal evolution of the vorticity field ω_x. The formation of coherent structures and subsequent turbulent decay are observed.

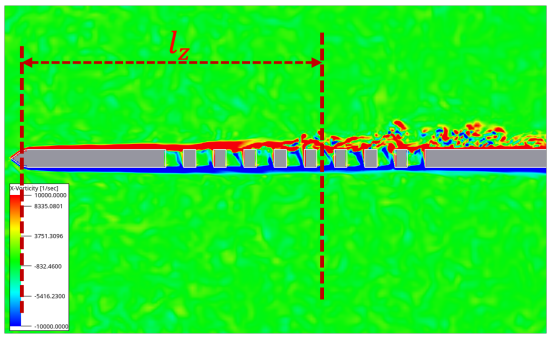

(a) Vortex shattering on the upper face

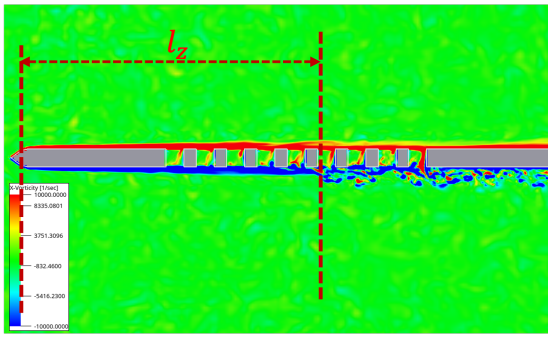

(b) Vortex shattering on the lower face

Figure 6.5: Spanwise vorticity

(Equation (4.7)), as detailed in Section 4.4. The calculation was performed at midspan ($x = 0$) by sampling the porous zone from $z/c = 0.129$ to $z/c = 0.365$, with a spatial/spectral resolution of $\Delta k = 44.3\,\mathrm{m}^{-1}$, where $\Delta k = 2/(N_z \cdot dz)$ (N_z being the number of sampling points and dz their reciprocal distance in the streamwise direction), and a frequency resolution of $\Delta f = 2.24\,\mathrm{Hz}$.

In Figure 6.6, the Frequency-wavenumber clearly shows the presence of a high-intensity lobe called the "Convective Ridge" [31], whose slope is equal to the convection velocity of the turbulent structures.
As indicated in the graph, this value is $0.35 \cdot U_\infty$, which is lower than the classical convection velocity of $0.7 \cdot U_\infty$. A reduction in convection velocity over porous materials was also identified by Damani et al. [16], who found a value closer to $0.48 \cdot U_\infty$ for the porous wall. In general, other

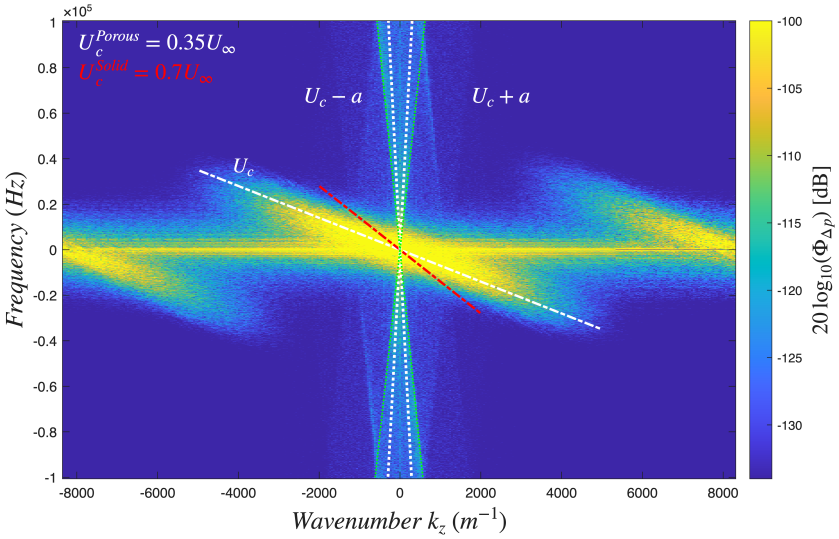

Figure 6.6: Frequency-Wavenumber Spectrum

studies have also demonstrated such a reduction on porous materials characterized by a reduced wall-blocking effect. Attributing this reduction solely to the increase in skin friction is premature since this parameter, as mentioned in the previous section, is still under heavy debate due to the numerous factors involved.
Indeed, an alternative mechanism for this reduction will be proposed.
It is worth recalling that the velocity of space-time waves can be either a *group velocity or a phase velocity*. Conceptually (referring to specific texts for formal definitions), the phase velocity is the "classical" indicator of the phase of a monochromatic wave characterized by a single frequency and a single wavelength, and it is evaluated as $\nu_p = \omega(k)/k$. The group velocity, instead, is defined when dealing with a wave packet characterized by at least two harmonics with different frequencies and wavelengths that give rise to an amplitude varying in space and time; it is evaluated as $\nu_g = \Delta\omega/\Delta k = d\omega/dk$. The velocity associated with the convection ridge is the group velocity. Moreover, Figure 6.6 shows how the convective ridge is characterized by distinctly blurred contours (green-blue) as it moves from the white line (yellow zone) towards the red one. This result was also highlighted by Damani et al. [16], who, in studying porous materials, observed a blurred transition from the group velocity—which characterizes the convective ridge—to the phase velocity, which characterizes the remaining regions, including the acoustic cone. This much more gradual transition, compared to a solid surface, indicates waves that travel faster, likely due to a more intense scattering effect than that found on smooth walls. Further insight into the mechanism would be obtained by comparing the results of this investigation with the ones obtained for a solid flat plate. Figure 6.6 also shows the near-field acoustic scattering [31] within the cone positioned centrally in the figure, delimited by the two white dashed lines with slopes $\nu_p = Uc \pm a$, where a is the speed of sound. The green dashed lines instead represent another high-intensity zone, greater than the acoustic one, but inclined with a slope $\nu_p \approx Uc \pm 0.5 \cdot a$
For an acoustic wave to propagate in far field, the phase velocity of the pressure jump generated by a rigid body must be at least equal to the speed of sound [23] (which is why an acoustic cone is defined); consequently, everything outside the white cone (referring to Figure 6.6) may be relevant in the near field but not in the far field.
This result could be consistent with the interpretation provided in the reference experimental work by Palleja-Cabre et al. [52].
Indeed, he defines the "cut-off" phenomenon as a possible acoustic reduction mechanism capable of developing only over the porous zone, characterized by a phase velocity equal to the convection velocity. These particular wavenumbers are well-known in literature as "evanescent modes" and are referred to near field acoustic waves which are unable to propagate in far field. In fact, it would seem that a large part of the acoustic energy that could be used for propagation is injected into modes with low phase velocity, thus at a subcritical speed and ultimately evanescent.
In order to illustrate a possible mechanism for the reduction of the convection velocity, Figure 6.7 shows the streamwise velocity profiles and the Reynolds stress $\overline{-u'v'}$, which are factors that

constitute the turbulent kinetic energy production term $\mathcal{P}$. This term appears within the turbulent kinetic energy equation—reported in its 2D form in Appendix B B.1—alongside the convective transport, dissipation, and diffusion terms. A study of this equation can provide an indication of the mechanism leading to a reduction in the convection velocity.

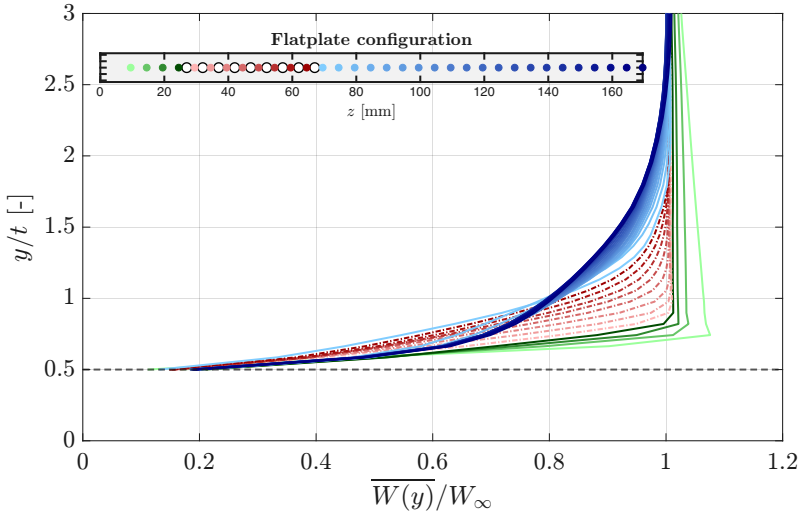

(a) streamwise velocity profiles

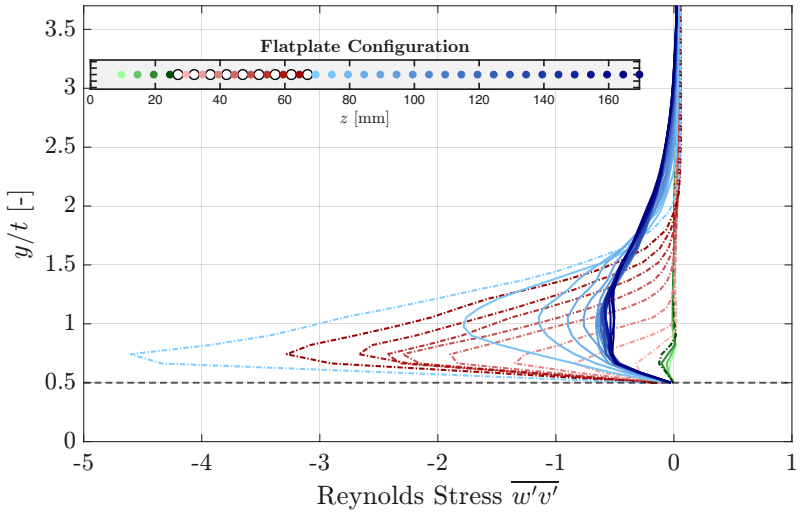

(b) Reynolds Stress $\overline{-wv}$

Figure 6.7: Turbulent kinetic energy production terms

Figure 6.7 provides a clear idea of the evolution of the boundary layer and its turbulent characteristics before the porous zone (solid green lines), through it (dashed red lines), and after the porous zone (solid blue lines). Each colored band transitions from light to dark as it approaches the adjacent study area.

Moving from the leading edge in the streamwise direction, a reduction in both the velocity and the wall-normal velocity gradient is observed in the near-wall regions until the exit of the porous zone; subsequently, both the velocity and the gradient start to increase again (blue lines). The Reynolds stress, conversely, increases within the porous zone and then decreases, reaching a plateau outside this area. The simplest explanation could be the increase in wall skin friction induced by the presence of the holes and the consequent energy dissipation due to friction. In reality, this hypothesis is to be excluded or relegated to a low-impact role, both because velocity gradients are reduced over the porous zone and because any form of dissipation ϵ is irreversible; therefore, if the velocity increases again downstream of the porous zone, the energy must have been transformed but not dissipated.

The porous zone, therefore, tends to reduce the kinetic contribution of the mean field, shifting energy toward the fluctuating field (turbulent field). This would also justify the reduction of

wall-blocking and the strong contribution of the vertical fluctuation RMS observed previously. Downstream of the porous zone, the fluctuating field is attenuated, and its energy contribution is transferred back to the mean flow. These shifts are carried out through diffusive processes acting both crosswise and streamwise; in fact, the blue profiles show maxima that are much more distributed even at high y coordinates.
It is worth highlighting that the term of turbulent kinetic energy production is not being assumed constant.

6.3 Study on phase shift

Once the convective velocity was evaluated, the $e^{i\pi}$ phase shift mechanism induced by porosity, was investigated.
The previous section highlighted the different intensities of harmonics related to hydrodynamics compared to those related to acoustics in the near field; therefore, in a similar manner, an attempt was made to understand the role of these two components in generating the phase shift, following the approach used by Shubham et al. [62].
To decompose the hydrodynamic and acoustic contributions in the near field, a filtering technique using a top-hat filter in the Fourier space was employed, as described in Section 4.4.

Unlike the study of Shubham et al. [62] and as described in Section 4.4, this thesis work does not strictly require the separation of the two acoustic components, thus following the procedure also adopted by Kang and Lee [40]. Following the decomposition, the results can be summarized in the images in Figure 6.8, where a straight line with the correct slope (velocity) is reported to demonstrate a successful decomposition.

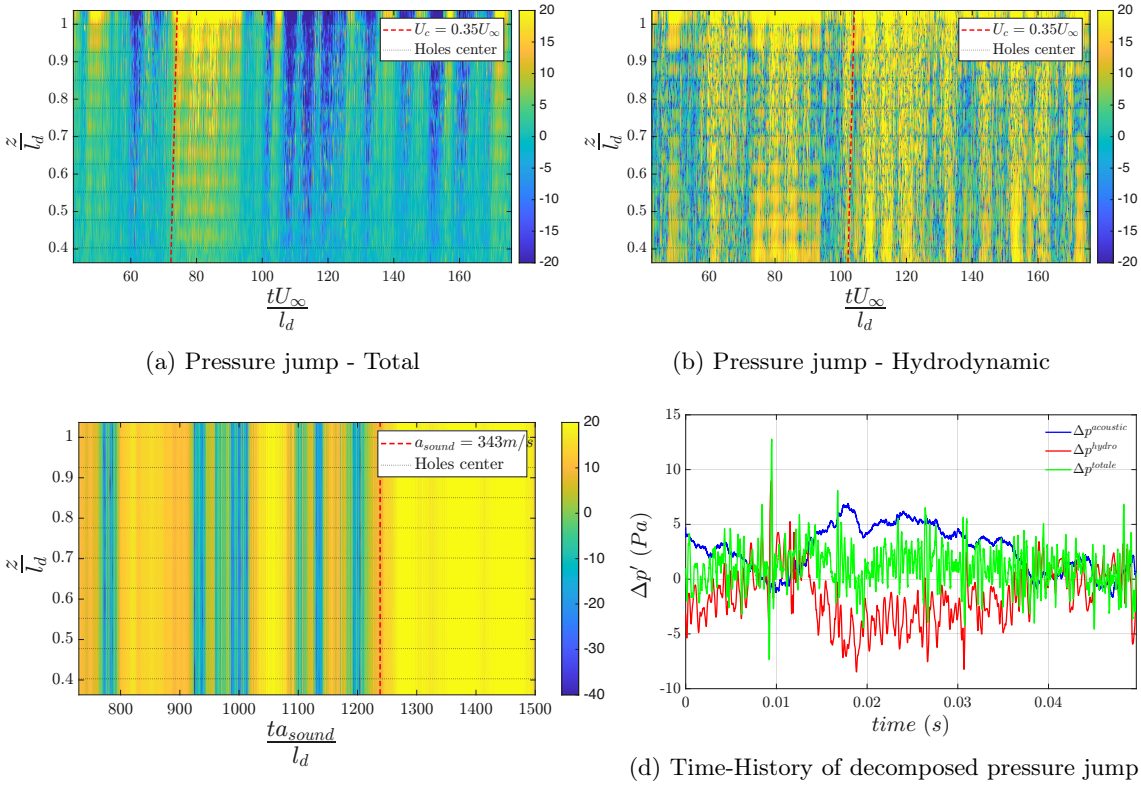

(a) Pressure jump - Total

(b) Pressure jump - Hydrodynamic

(c) Pressure jump - Acoustic

(d) Time-History of decomposed pressure jump Δp (reduced time window)

Figure 6.8: Decomposition results

Comparing Fig. 6.8b and Fig. 6.8c, a streamwise-oriented high-energy and intermittent structure can be observed in the former, as also highlighted in Kang and Lee [40]. Meanwhile, the presence of these structures is evident in both the total pressure jump component in Fig. 6.8a and the hydrodynamic component in Fig. 6.8b, demonstrating that the hydrodynamic component plays a fundamental role in the total fluctuation. In Fig. 6.8d, we find the temporal evolution of the decomposed pressure jumps for a generic time window. Unlike what is found in the literature

and what might be expected, the values assumed by the acoustic pressure jump are not negligible compared to the hydrodynamic ones. This characteristic is reasonable since the fluctuations of the pressure jump are being evaluated, rather than simple pressure fluctuations, given our interest in the load on the flat plate.
Having an $\Delta p^{acoustic}$ comparable to Δp^{hydro} justifies having decomposed the components and carried out the shifting analysis only on the hydrodynamic component, since the acoustic component is in no way involved in the phase shift, as we'll see later.

To understand the roles of the hydrodynamic and acoustic components in the phase shift $\theta_{\Delta p}$ after performing the decomposition, the Cross-Power Spectral Density (CPSD) $G_{\Delta p \Delta p}$ was evaluated using Equation (4.12) as described in Section 4.4.

The CPSD is evaluated between a reference signal (from here on, $\Delta p'$ is implied) located in the immediate vicinity of the Leading Edge — indicated by a green square in Figure 6.10 — and those within the porous zone, all sampled at the midspan.

The phase shift was evaluated as $\Re(e^{i\theta_{\Delta p}})$ such that values close to 1 indicate that the two wall-pressure signals are in-phase, while values close to –1 signify an out-of-phase relationship. In the images presented below, a red arrow indicates the streamwise coherence length l_z, evaluated with respect to the reference sampling point (green square) as in Equation (4.13) as highlighted in Section 4.4.

The idea of evaluating the coherence length instead of the integral length scale is supported when dealing with aeroacoustics, according to Tian and Lyu [67].
Figure 6.9 shows the trend of $l_z(\omega)$ to which the abscissa relative to the point where the correlation length was evaluated (i.e., the z coordinate of the green square in Figure 6.10), has been added. The value considered is the one related to the unitary Strouhal number, both because it is higher than the others and because it corresponds to the main harmonic.
As explained subsequently, we are interested in the maximum value of the coherence length as it represents the ultimate value beyond which the influence of the pressure jump at the Leading Edge no has any effect.

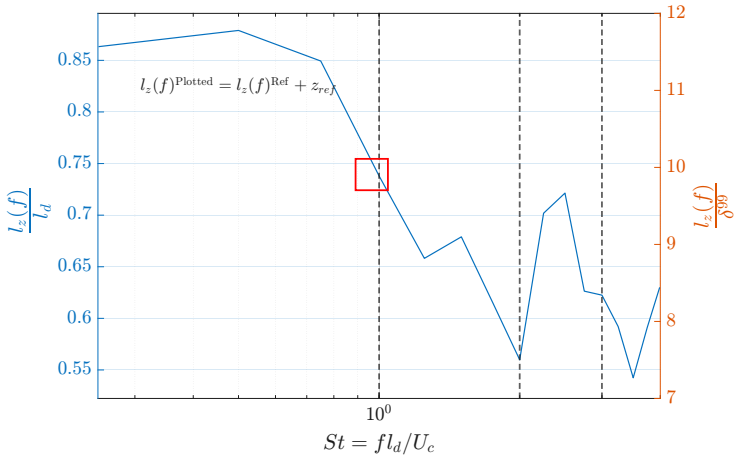

Figure 6.9: Streamwise coherence length

Figure 6.10, which shows the phase angle of $e^{\omega \Delta z/U_c} + e^{i\pi}$, clearly illustrates that the acoustic component plays no role in the phase shift, in agreement with the observations of Kang and Lee [40]. Conversely, the hydrodynamic component exhibits wide frequency intervals where a phase shift is present. This separation of contributions is fundamental, as it allows for a focus solely on the hydrodynamic component.
Although the phase shift—and thus a possible destructive interference—is present, the occurrence of phase shifts at integer St values requires a more refined analysis proposed below.
According to the study by Palleja-Cabre et al. [52], the phase shift as a mechanism for noise reduction consists of two components:

1. $e^{\omega \Delta z/U_c}$, which is a phase delay induced by the different location of the acoustic sources on the flat plate relative to the source at the Leading Edge. Indeed, Δz stands for $z_i - z_{LE}$;

2. $e^{i\pi}$, which is responsible for shifting the reduction peaks toward integer Strouhal numbers,

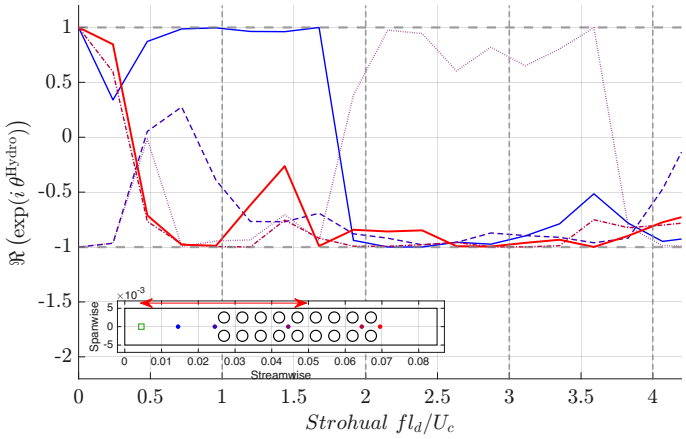

(a) Phase shift of hydrodynamic pressure jump

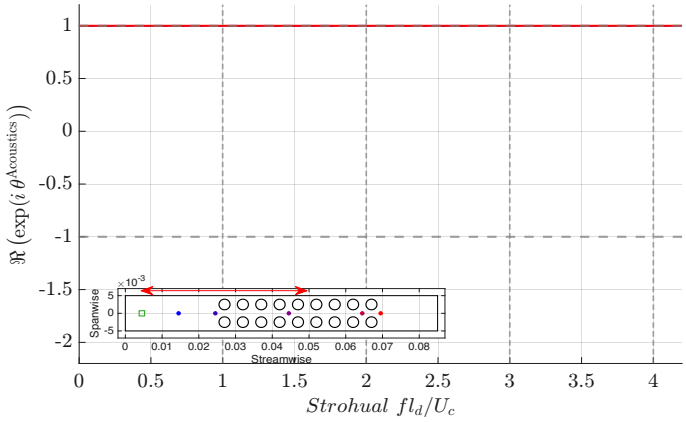

(b) Phase shift of acoustics pressure jump

Figure 6.10: Hydrodynamic and Acoustic Phase Shift ($e^{i\pi} + e^{\omega\Delta z/U_c}$)

also according to Chaitanya et al. [9].

While the interference due to phase delay is typical of any source with an extension greater than a point, the phase opposition is typical of the presence of porosity; therefore, it will be necessary to analyze it in detail, splitting the two contributions.

To understand the effect of the two types of phase shift, θ^{hydro} is reported both by isolating the phase shift, due to phase delay, and by showing the sum of the two contributions in Figure 6.11, where it is clearly seen how the combined contribution of the two shifts builds a phase opposition contribution that is not frequency-dependent, especially at the final points of the porosity.
Having separated the two contributions, it is possible to understand the effect of porosity and thus the $e^{i\pi}$ phase shift through Figure 6.12, where the hydrodynamic component phase shifts are shown in relation to the streamwise coherence length of the pressure jump, represented by the red arrow.

The phase shifts of points within the coherence length (see Figure 6.12a), do not show any periodicity at integer St. In contrast, for phase shifts sampled at points outside the coherence length (see Figure 6.12b), a clear structure emerges. Specifically, even starting from the first point in Figure 6.12b, a structure with numerous peaks at integer Strouhal numbers is present, which tends to be refined as we proceed toward the exit of the porous zone. In order to point out the good agreement of phase shifting peak are with integer strohual, Figure 6.13 displays the phase shifting of the last 3 points. The role of the streamwise coherence length, although requiring further investigation, represents the distance beyond which the effects of the pressure jump at the leading edge become negligible, allowing the porous section to fully manifest its phase inversion properties. This phase shifting, outside of streamwise coherence length, seems to be in accordance with the vortex shattering in figure 6.5 where, outside of l_z, there is an heterogeneous vorticity induced by turbulent structure breaking and by penetration of vorticity —developed on one side of the flat

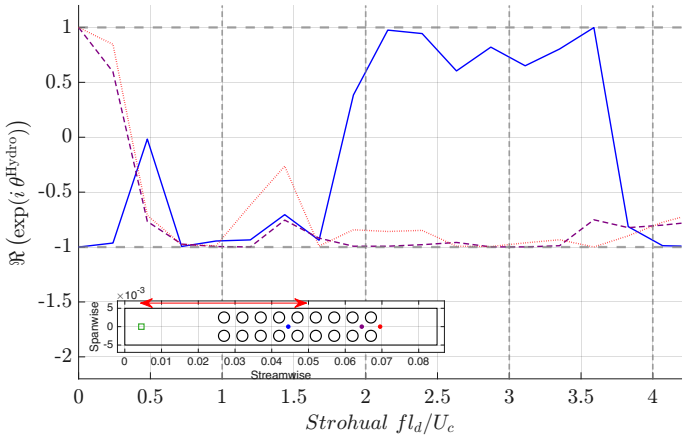

(a) $e^{i\pi} + e^{\omega\Delta z/U_c}$

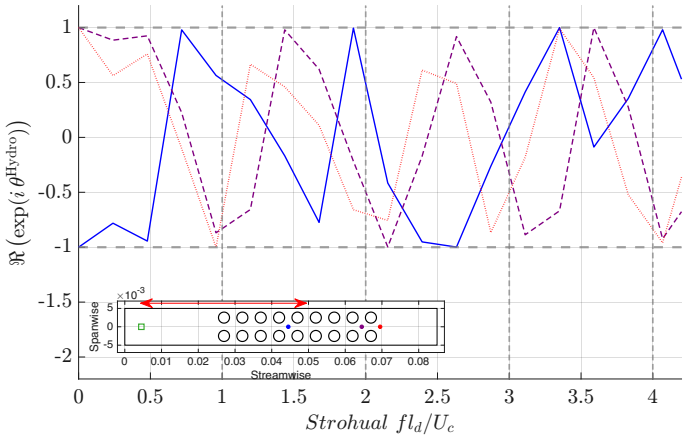

(b) $e^{i\pi}$

Figure 6.11: Hydrodynamic Phase Shift

plate—onto the opposite face through the pores. Within the coherence length, however, the pores appear to be obstructed by a stable and "compact" boundary layer, which almost entirely shields them from the incoming flow. This concept is supported by Figure 6.14, in which no compact sources are visible at the entrance of the porous zone, thereby confirming the analytical model proposed by Palleja-Cabre et al. [52]. In other words, the presence of a compact boundary layer at the leading edge of the porous region creates an extension of the solid surface; this prevents the impedance changing that would otherwise trigger the formation of a compact source.

It is worth noting that the phase-shift peaks $e^{i\pi}$ occurring at integer Strouhal numbers exhibit a frequency dependence, in contrast to the observations reported in the experimental work by Palleja-Cabre et al. [52]. However, this is not the case for the total phase-shift contribution ($e^{i\pi}+e^{i\omega\Delta z/U_c}$), which, as shown in Figure 6.11, appears to maintain phase opposition regardless of the frequency.

6.4 Directivity pattern

Figure 6.15 shows the directivity pattern for different values of the Strouhal number S_t. This plot is obtained by evaluating the acoustic spectra (resolution frequency equal to $0.25 \cdot \Delta S_t$) of far-field acoustic pressure values extracted via acoustic analogy from the microphones positioned to form a circle of radius $R = 1.17m$, centred at the midspan of the leading edge.

The dipolar nature is clearly evident, since the acoustic production is associated with pressure jumps and thus with forces applied to the flat plate. Furthermore, the tilt of the lobes is highlighted, resulting from flow convection, which is well known in analytical formulations as

$$[1 - M_s \cdot \cos(\theta)]^{-4}$$

where M_s is the acoustics source Mach number.

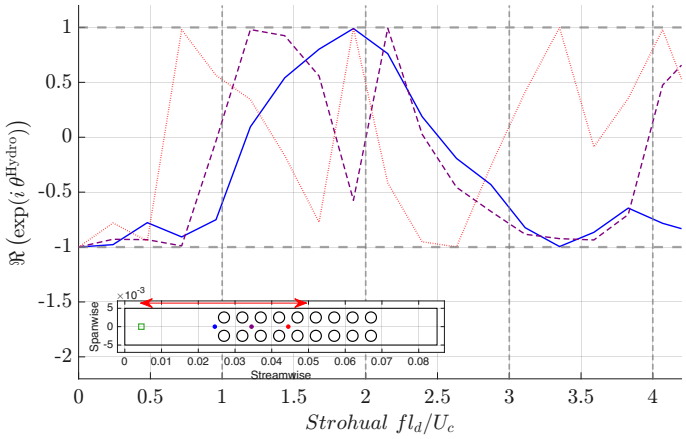

(a) Phase shift inside of the streamwise coherence length

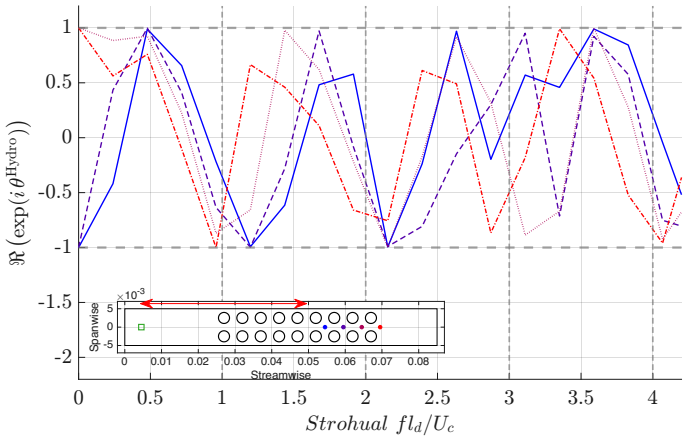

(b) Phase shift outside of the streamwise coherence length

Figure 6.12: Phase shifting in relation to the streamwise coherence length

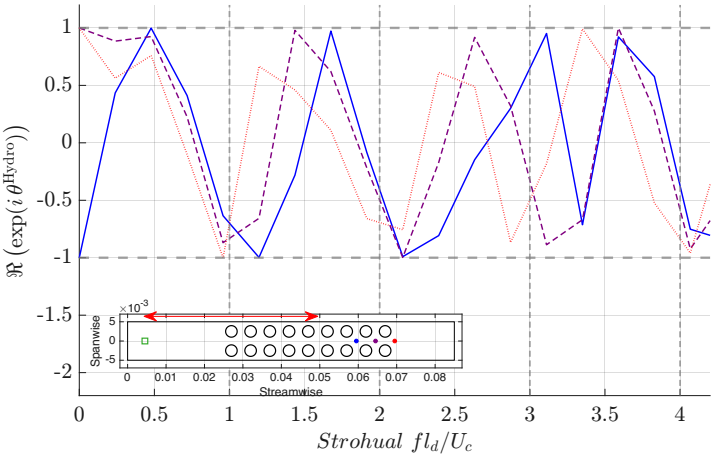

Figure 6.13: Hydrodynamic phase shift for the last three sampled points

A much more unusual aspect is the different inclination of the lobes, as those referring to integer S_t show a smaller, or at most equal, inclination compared to those at non-integer S_t. A hypothesis in this regard could be traced back to the cut-off effect: a reduction in the convection velocity of the acoustic wave affects M_s, altering the convective amplification. However, this interpretation remains a hypothesis that will require further and more detailed analysis, also to exclude any dependence on the windowing of Welch's method.

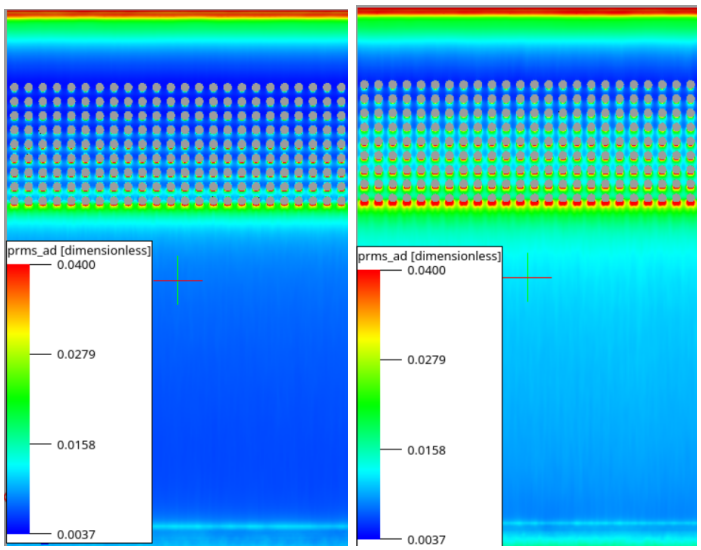

Figure 6.14: Contours of the no-dimensional RMS of the pressure surface $p_{rms}/\rho_\infty U_\infty^2$ on both sides

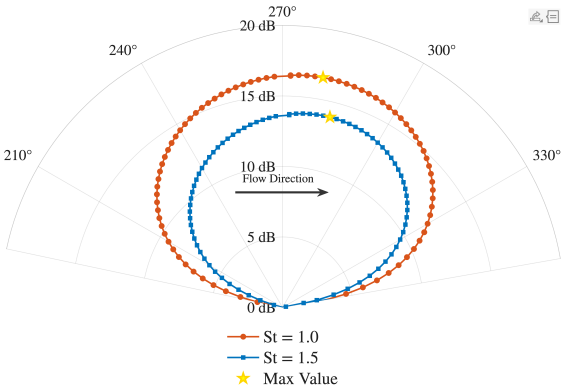

(a) S_t=1 and S_t=1.5

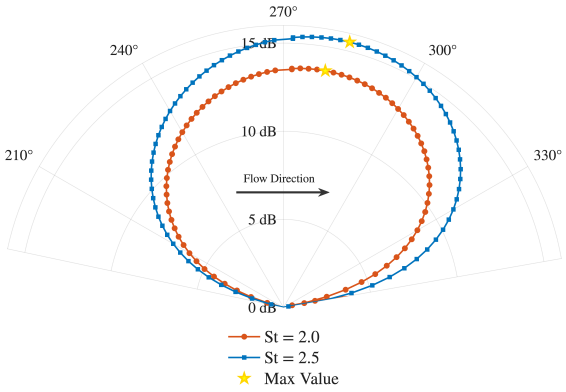

(b) S_t=2 and S_t=2.5

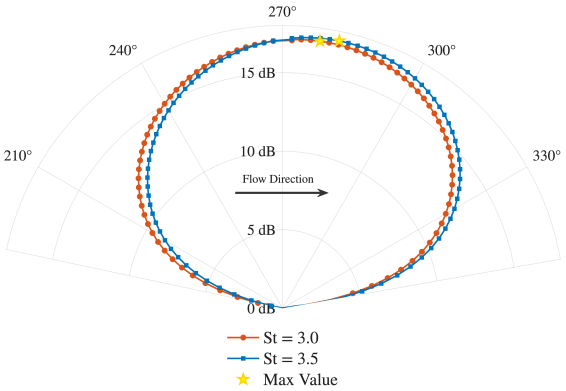

(c) S_t=3 and S_t=3.5

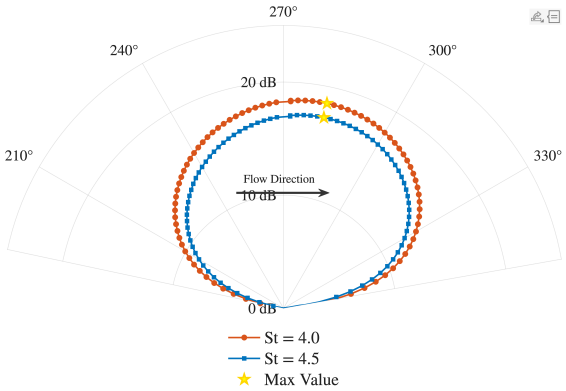

(d) S_t=4 and S_t=4.5

Figure 6.15: Directivity Pattern

Chapter 7

Conclusion

"E quindi uscimmo a rivedere le stelle."
— *Dante Alighieri, Divina Commedia, Inferno*

This thesis work aims to numerically investigate the noise-reduction mechanisms associated with the introduction of downstream porosity on a flat plate, with the objective of extending the previous experimental work conducted by Palleja-Cabre et al. [52]. The latter demonstrated the presence of acoustic reduction peaks at integer Strouhal numbers, defined as $St = f \cdot l_d/U_c$, where l_d is the distance between the end of the porous section and the leading edge, f is the frequency, and U_c is the convection velocity.

Specifically, the present study focuses on two of the mechanisms proposed by Palleja-Cabre et al. [52]: the evanescent modes (also referred to as cut-off modes)—harmonics characterized by a subcritical phase velocity and thus unable to propagate into the far field—and the phase shift between the pressure jump measured at the leading edge and those across the porous zone. In the aforementioned experimental work, this latter mechanism was attributed to counter-rotating secondary vorticity induced by the interaction of the primary vortex with the wall.

Two significant results have emerged from this research. The first pertains to the presence of near-field acoustic harmonics associated with a propagation speed, significantly lower than the speed of sound, also known as subcritical speed. These harmonics, which carry greater acoustic energy than those propagating at the speed of sound, appear to represent the cut-off phenomenon indicated in the experimental activity. Furthermore, it is noteworthy that porosity is capable of reducing not only the propagation speed of these acoustic modes but also the turbulence convection velocity, which decreases by approximately 65% compared to the freestream velocity.

The second outcome pertains to the decomposition between near-field acoustics and hydrodynamics. It is highlighted that the phase shift is primarily a hydrodynamic feature, capable of generating destructive interference that ensures a reduction in acoustic emissions. The key finding was the presence of phase-shift peaks between the hydrodynamic waves related to the pressure jump at the leading edge and those across the porous zone, downstream of the coherence length l_z. These peaks occur exactly at integer Strouhal numbers, where acoustic reduction peaks were measured in the far field.

A frequency-dependent phase-shift term is a completely novel result compared to the experimental-analytical model, which assumed a constant term. This mechanism has been attributed to highly heterogeneous vorticity over the pores downstream of l_z, induced by the collapse of Kelvin-Helmholtz waves triggered by the upwash and downwash mechanisms within the pores—thus, a highly non-linear mechanism not captured by the analytical model.

Research in this field is undoubtedly complex and necessitates further analysis, beginning with an in-depth study of the subcritical velocities that characterize evanescent modes. It will be essential to perform direct comparisons with results from solid flat-plate simulations to fully grasp the underlying concept of the phase shift. Although it has been established that the noise reduction peaks at integer Strouhal numbers are attributable to hydrodynamic factors, this mechanism must be linked more directly to the actual noise reduction to understand how these phase shifts influence the far field. One hypothesis is that these phase shifts are not present in the far-field acoustics

themselves, but rather act as a destructive fluid-dynamic mechanism that suppresses acoustic emission at specific frequencies.

Finally, a detailed study of aeroacoustic feedback mechanisms is highly recommended, given the atypical behavior of the acoustic and hydrodynamic pressure jumps described previously.

Appendix A

First Appendix

"Fa' beni e scordatillu, fà mali e pensaci"

— *DETTO SICILIANO*

The study conducted in this thesis led to several results that were non-dimensionalized using the boundary layer thickness (the value where $V_z(y) = 0.99 \cdot V_\infty$) and the boundary layer displacement thickness, calculated as A.1:

$$\delta^* = \int_0^h \left(1 - \frac{U(y)}{U_\infty}\right) dy \tag{A.1}$$

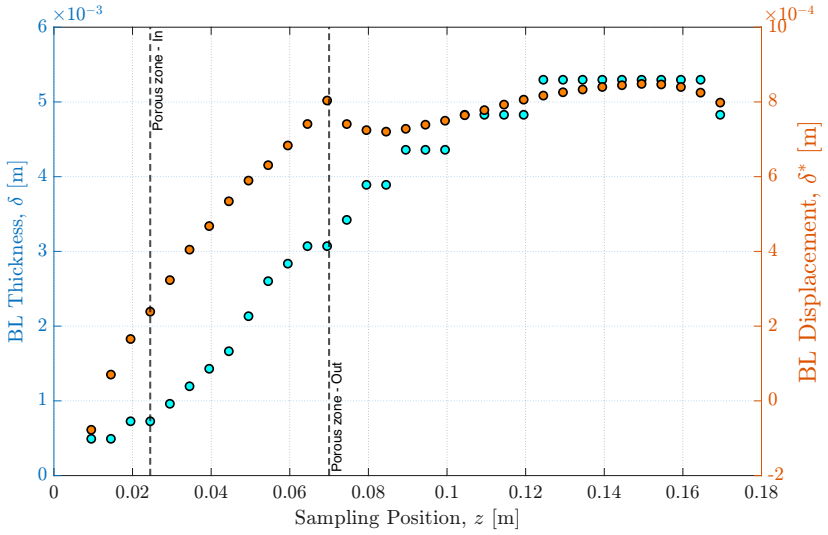

Figure A.1: Boundary layer features

The obtained values are summarized in the graph in Figure A.1, where it can be observed that both characteristics under examination increase until reaching a plateau downstream of the porous zone. For this reason, in order to decouple the analysis from this variability, the reference parameter adopted was the value reached approximately between 0.12 m and 0.17 m, which is roughly 5 mm e 0.8 mm for δ e δ^* respectively .

Appendix B

Second Appendix

"Cercate l'accordo di dominante corretto al vostro accordo di tonica"

—

Assuming the boundary layer approximation applied to a flow that is steady and two-dimensional in the mean, the Turbulent Kinetic Energy (TKE) equation reduces to:

$$\underbrace{\frac{1}{2}U\frac{\partial\left(\overline{q^2}\right)}{\partial x}+\frac{1}{2}V\frac{\partial\left(\overline{q^2}\right)}{\partial y}}_{\mathcal{C}}=\underbrace{-\overline{uv}\frac{\partial U}{\partial y}}_{\mathcal{P}}\underbrace{-\frac{\partial}{\partial y}\left(\frac{1}{2}\overline{q^2v}\right)}_{\mathcal{T}_k}\underbrace{-\frac{\partial}{\partial y}\left(\frac{1}{\rho}\overline{pv}\right)}_{\Pi}+\underbrace{\nu\overline{u_i\frac{\partial^2 u_i}{\partial x_j^2}}}_{\mathcal{D}_k+\epsilon_k} \tag{B.1}$$

where:

- $\mathcal{C}$ represents convection, or equivalently, the transport of turbulent energy by the mean flow;
- $\mathcal{P}$ denotes the production of turbulent energy through the interaction between the mean flow and turbulence. According to Tritton [68], this term represents the transfer of energy from the mean flow to the turbulence;
- $\mathcal{T}_k$ is the turbulent transport (or advective transport) of turbulent energy by the fluctuating motion;
- Π represents the transport of turbulent energy by pressure work;
- $\mathcal{D}_k+\epsilon_k$ are the viscous terms, consisting of the sum of viscous diffusion and viscous dissipation.

Bibliography

[1] Abou-Hussein, H., DeBenedictis, A., Harrison, N., Kim, M., Rodrigues, M. A., Zagadou, F., and Howe, M. S. (2002). Vortex-surface interaction noise: A compendium of worked examples. *Journal of Sound and Vibration*, 252.

[2] Andersson, M. and Karlsson, M. (2021). Characterization of anisotropic turbulence behavior in pulsatile blood flow. *Biomechanics and Modeling in Mechanobiology*, 20:1–16.

[3] Blackmore, T., Batten, W. M., and Bahaj, A. S. (2013). Inlet grid-generated turbulence for large-eddy simulations. *International Journal of Computational Fluid Dynamics*, 27(6-7):307–315.

[4] Breugem, W. P., Boersma, B. J., and Uittenbogaard, R. E. (2006). The influence of wall permeability on turbulent channel flow. *Journal of Fluid Mechanics*, 562:35–72.

[5] Brooks, T. F., Pope, D. S., and Marcolini, M. A. (1989). Airfoil self-noise and prediction. Technical Report NASA Reference Publication 1218, NASA Langley Research Center, Hampton, Virginia, USA.

[6] Brown, A. L. and van Kamp, I. (2017). Who environmental noise guidelines for the european region: A systematic review of transport noise interventions and their impacts on health. *International Journal of Environmental Research and Public Health*, 14(8):873.

[7] Casalino, D., Grande, E., Romani, G., Ragni, D., and Avallone, F. (2021). Definition of a benchmark for low reynolds number propeller aeroacoustics. *Aerospace Science and Technology*, 113.

[8] Chaitanya, P., Joseph, P., Chong, T. P., Priddin, M., and Ayton, L. (2017). On the noise reduction mechanisms of porous aerofoil leading edges. *Journal of Sound and Vibration*, 404:18–33.

[9] Chaitanya, P., Joseph, P., Chong, T. P., Priddin, M., and Ayton, L. (2020). On the noise reduction mechanisms of porous aerofoil leading edges. *Journal of Sound and Vibration*, 485.

[10] Chattopadhyay, N. C., Salam, A., Tasnim, N., and Hossain, A. B. (2013). Role of chevrons in engine noise control. *MIST International Journal of Science and Technology*, 2(1):61–68. Military Institute of Science and Technology (MIST).

[11] Chen, H., Chen, S., and Matthaeus, W. (1992a). Recovery of the navier-stokes equations using a lattice-gas boltzmann method. *Physical Review A*, 45.

[12] Chen, H., Chen, S., and Matthaeus, W. H. (1992b). Recovery of the navier-stokes equations using a lattice-gas boltzmann method. *Phys. Rev. A*, 45:R5339–R5342.

[13] Chen, H., Zhang, R., Gopalakrishnan, P., Li, Y., Fares, E., and Casalino, D. (2016). Recent advances of the lattice boltzmann method for transonic flow. In *Conference Presentation*.

[14] Chin, J. (2005). *Mesoscale fluid simulation with the Lattice Boltzmann method*. PhD thesis, Queen Mary University of London.

[15] Criminale, W. O., Jackson, T. L., and Joslin, R. D. (2003). *Theory and Computation of Hydrodynamic Stability*. Cambridge University Press, Cambridge.

[16] Damani, S., Totten, E., Butt, H., Sharma, B., Devenport, W. J., and Lowe, K. T. (2025). Comparison of sub-convective pressure fluctuations over a smooth and rough wall. *International Journal of Heat and Fluid Flow*, 115:109835.

[17] Drazin, P. G. and Reid, W. H. (1981). *Hydrodynamic Stability*. Cambridge University Press, Cambridge.

[18] Envia, E. (2001). Fan noise reduction: An overview. In *39th AIAA Aerospace Sciences Meeting and Exhibit*, AIAA Paper 2001-0661, Reno, NV, USA. American Institute of Aeronautics and Astronautics.

[19] European Commission (2021). Communication from the commission to the european parliament, the council, the european economic and social committee and the committee of the regions: Pathway to a healthy planet for all – eu action plan: 'towards zero pollution for air, water and soil'. Communication COM(2021) 400 final, European Commission, Brussels, Belgium.

[20] European Commission, Directorate-General for Environment, VITO, TNO, and IIASA (2021). Assessment of potential health benefits of noise abatement measures in the eu: Phenomena project. Technical Report 07.0203/2019/ETU/815591/ENV.A.3, European Commission, Brussels, Belgium.

[21] European Environment Agency (2020). Environmental noise in europe — 2020. Technical Report 22/2019, European Environment Agency (EEA), Luxembourg.

[22] European Environment Agency (2025). Environmental noise in europe 2025. EEA Report 05/2025, European Environment Agency, Copenhagen, Denmark.

[23] Fahy, F. and Gardonio, P. (2007). *Sound and Structural Vibration: Radiation, Transmission and Response*. Academic Press (Elsevier), London, 2nd edition.

[24] Farassat, F. (2007). Derivation of formulations 1 and 1a of farassat. Technical report.

[25] Feng, Z. and Ye, Q. (2023). Turbulent boundary layer over porous media with wall-normal permeability. *Physics of Fluids*, 35(9):095111.

[26] Ferziger, J. H. and Perić, M. (2002). *Computational Methods for Fluid Dynamics*. Springer, Berlin, third edition.

[27] Ferziger, J. H., Peric, M., and Leonard, A. (1997). Computational methods for fluid dynamics. *Physics Today*, 50.

[28] Filippone, A. (2014). Aircraft noise prediction. *Progress in Aerospace Sciences*, 68:27–63.

[29] Francesca Tosi, Prof. Luciano Misici, P. R. P. (2000-2001). Modelli "lattice boltzmann" e l'equazione di navier-stokes. Master's thesis, UNIVERSITÀ DEGLI STUDI DI CAMERINO.

[30] Geyer, T. F., Lucius, A., Schrödter, M., Schneider, M., and Sarradj, E. (2019). Reduction of turbulence interaction noise through airfoils with perforated leading edges. *Acta Acustica united with Acustica*, 105.

[31] Glegg, S. and Devenport, W. (2024). 12 - wall pressure fluctuations in turbulent boundary layers. In Glegg, S. and Devenport, W., editors, *Aeroacoustics of Low Mach Number Flows (Second Edition)*, pages 379–405. Academic Press, second edition edition.

[32] Gómez-de Segura, G. and García-Mayoral, R. (2019). Turbulent drag reduction by anisotropic permeable substrates – analysis and direct numerical simulations. *Journal of Fluid Mechanics*, 875:124–172.

[33] Grace, S. (2001). Unsteady blade pressure-the bvi model vs. the gust model. In *7th AIAA/CEAS Aeroacoustics Conference and Exhibit*, page 2209.

[34] Guha, A., Rahmani, M., and Lawrence, G. A. (2013). Evolution of a barotropic shear layer into elliptical vortices. *Physical Review E*, 87:013020.

[35] Herrmann, D. (2007-2008). A study of the suitability of powerflow as an educational engineering design tool for undergraduate students. Master's thesis, University of Colorado.

[36] Higuera, F. J., Succi, S., and Benzi, R. (1989). Lattice gas dynamics with enhanced collisions. *Europhysics Letters*, 9(4):345.

[37] Hinze, J. O. (1975). *Turbulence*. McGraw-Hill series in mechanical engineering. McGraw-Hill, New York.

[38] Jiang, C., Moreau, D., de Silva, C., and Doolan, C. (2024a). Noise generation mechanisms of a micro-tube porous trailing edge. *Journal of Sound and Vibration*, 571.

[39] Jiang, C., Moreau, D., de Silva, C., and Doolan, C. (2024b). Noise generation mechanisms of a micro-tube porous trailing edge. *Journal of Sound and Vibration*, 571:118085.

[40] Kang, D. and Lee, S. (2025). Role of hydrodynamic and acoustic pressures in trailing-edge noise using numerical and analytical approaches. *Phys. Rev. Fluids*, 10:034609.

[41] Kim, J. W., Haeri, S., and Joseph, P. F. (2016). On the reduction of aerofoil turbulence interaction noise associated with wavy leading edges. *Journal of Fluid Mechanics*, 792:526–552.

[42] Kuwata, Y. (2022). Role of spanwise rollers by kelvin–helmholtz instability in turbulence over a permeable porous wall. *Phys. Rev. Fluids*, 7:084606.

[43] Leishman, J. G. (2023). *Introduction to aerospace flight vehicles*. Embry-Riddle Aeronautical University.

[44] Merino-Martínez, R., Carpio, A. R., Pereira, L. T. L., van Herk, S., Avallone, F., Ragni, D., and Kotsonis, M. (2020). Aeroacoustic design and characterization of the 3d-printed, open-jet, anechoic wind tunnel of delft university of technology. *Applied Acoustics*, 170.

[45] Metin, C. and Ezan, M. A. (2020). Anti-hairpin vortices in the buoyancy-driven turbulent boundary layer.

[46] Narayanan, S., Chaitanya, P., Haeri, S., Joseph, P., Kim, J. W., and Polacsek, C. (2015). Airfoil noise reductions through leading edge serrations. *Physics of Fluids*, 27.

[47] NASA (2005). NASA's Chevron Technology Quiets the Skies. `https://www.nasa.gov/centers-and-facilities/glenn/nasas-chevron-technology-quiets-the-skies/`. Accessed: 2026-03-03.

[48] Nieuwstadt (†), F., Boersma, B., and Westerweel, J. (2016). *Turbulence: Introduction to Theory and Applications of Turbulent Flows*. Springer, United States.

[49] Nosrati, K., Rahm Rahimpour, A., Afzalimehr, H., Nazari-Sharabian, M., and Karakouzian, M. (2024). Experimental investigation of anisotropic invariants in streams with rigid vegetation and 3d bedforms. *Fluids*, 9(12).

[50] Ocker, C., Czwielong, F., Geyer, T. F., Chaitanya, P., Merkel, M., and Becker, S. (2021a). Permeable structures for leading edge noise reduction. In *AIAA Aviation and Aeronautics Forum and Exposition, AIAA AVIATION Forum 2021*.

[51] Ocker, C., Geyer, T. F., Czwielong, F., Krömer, F., Pannert, W., Merkel, M., and Becker, S. (2021b). Permeable leading edges for airfoil and fan noise reduction in disturbed inflow. *AIAA Journal*, 59(10):4178–4193.

[52] Palleja-Cabre, S., Chaitanya, P., Joseph, P., Kim, J. W., Priddin, M. J., Ayton, L. J., Geyer, T. F., and Chong, T. P. (2022). Downstream porosity for the reduction of turbulence–aerofoil interaction noise. *Journal of Sound and Vibration*, 541.

[53] Paruchuri, C. (2017). *Aerofoil geometry effects on turbulence interaction noise*. Doctoral thesis, University of Southampton, Faculty of Engineering and the Environment, Institute of Sound and Vibration Research, Southampton, United Kingdom.

[54] Paruchuri, C., Joseph, P., and Ayton, L. (2020). Leading edge profiles for the reductions of aerofoil interaction noise. *AIAA Journal*.

[55] Piccolo, A., Zamponi, R., Avallone, F., and Ragni, D. (2024). Turbulence distortion and leading-edge noise. *Physics of Fluids*, 36(12):125183.

[56] Priddin, M., Ayton, L., Cabre, S. P., Paruchuri, C., and Joseph, P. (2021). Downstream perforations for the reduction of turbulence-aerofoil interaction noise: Part ii - theoretical investigation. In *AIAA AVIATION 2021 FORUM*.

[57] Qin, Z., Fang, L., and Fang, J. (2016). How isotropic are turbulent flows generated by using periodic conditions in a cube? *Physics Letters A*, 380(13):1310–1317.

[58] Roach, P. (1987). The generation of nearly isotropic turbulence by means of grids. *International Journal of Heat and Fluid Flow*, 8(2):82–92.

[59] Roache, P. J. (1997). Quantification of uncertainty in computational fluid dynamics. *Annual Review of Fluid Mechanics*, 29:123–160.

[60] R.Verzicco, M.de.Tullio, G. I. (VKI, May 13-17 2024). Lecture series on les and related techniques: Theory and applications. In *Immersed Boundary Techniques for Large Eddy Simulation*.

[61] Seo, J. H. and Moon, Y. (2007). Aerodynamic noise prediction for long-span bodies. *Journal of Sound and Vibration*, 306:564–579.

[62] Shubham, S., Sandberg, R. D., Moreau, S., and Wu, H. (2022). Surface pressure spectrum variation with mach number on a cd airfoil. *Journal of Sound and Vibration*, 526:116762.

[63] Simonsen, A. J. and Krogstad, P.- (2005). Turbulent stress invariant analysis: Clarification of existing terminology. *Physics of Fluids*, 17(8):088103.

[64] Teruna, C. (2022). *Aerodynamic Noise Reduction with Porous Materials: Aeroacoustics Investigations and Applications*. PhD thesis, Delft University of Technology, Delft, Netherlands. Research Group: Wind Energy.

[65] Tewari, K., Dewan, A., Narayanan, V., and Dogra, G. (2021). Large eddy simulation of passive noise reduction in subsonic jets by using chevrons. In *Proceedings of the 14th International Conference on Mechanical Engineering (ICME 2021)*, Dhaka, Bangladesh. Affiliations: IIT Delhi and IIT Gandhinagar.

[66] The World Bank (2017). Urban population (% of total). `https://data.worldbank.org/indicator/SP.URB.TOTL.IN.ZS`. Data retrieved from World Bank Open Data.

[67] Tian, H. and Lyu, B. (2024). The impact of non-frozen turbulence on the modelling of the noise from serrated trailing edges. *Journal of Fluid Mechanics*, 990.

[68] Tritton, D. J. (1977). *Physical Fluid Dynamics*. Springer (The Modern University in Physics Series), Dordrecht, 1 edition.

[69] Turner, J. M. and Kim, J. W. (2020). Trailing-edge noise generation from a flat-plate aerofoil interacting with a prescribed vortex. *Journal of Sound and Vibration*, 489:115654.

[70] University of Washington (n.d.). Fluent k– model notes. `https://courses.washington.edu/mengr544/handouts-10/Fluent-k-epsilon.pdf`. Lecture handout, ME 544: Advanced Fluid Turbulence, Department of Mechanical Engineering, University of Washington.

[71] WHO Regional Office for Europe and Joint Research Centre (2011). *Burden of disease from environmental noise: Quantification of healthy life years lost in Europe*. World Health Organization Regional Office for Europe, Copenhagen, Denmark.

[72] Xu, D. and Chen, J. (2013). Accurate estimate of turbulent dissipation rate using piv data. *Experimental Thermal and Fluid Science*, 44:662–672.

[73] Zagvozdina, K. and Burovski, E. (2021). Exploring the accuracy of the lattice boltzmann method. *Journal of Physics: Conference Series*, 1740(1):012027.

[74] Zamponi, R., Moreau, S., and Schram, C. (2021). Rapid distortion theory of turbulent flow around a porous cylinder. *J. Fluid Mech.*, 915:A27.

[75] Zamponi, R., Satcunanathan, S., Moreau, S., Meinke, M., Schröder, W., and Schram, C. (2023). Effect of porosity on Curle's dipolar sources on an aerofoil in turbulent flow. *J. Sound Vib.*, 542:117353.

[76] Zamponi, R., Satcunanathan, S., Moreau, S., Ragni, D., Meinke, M., Schröder, W., and Schram, C. (2020). On the role of turbulence distortion on leading-edge noise reduction by means of porosity. *Journal of Sound and Vibration*, 485:115561.